Massively Parallel Simulations of Coupled Arterial Cells: Ca^{2+} Dynamics and Atherosclerosis

---

Student:

Stewart Edward Dowding

Supervisors:

Prof. Tim David

Dr. Constantine Zakkaroff

A thesis submitted in partial fulfilment of the requirements for the Degree of Master of Engineering in Bioengineering

at the

University of Canterbury

February 24, 2017

Contents

List of Figures

Acknowledgements

First and foremost, I wish to express my sincere gratitude to my supervisors Prof. Tim David and Dr. Constantine Zakkaroff. You have both taught me a great deal and provided an incredible amount of support during my research. I would also like to thank University of Canterbury High Performance Computing for funding much of the work presented in this thesis, and for providing such a positive environment to work in. It was a privilege to get to know the wonderful people here over the past couple of years—thank you all.

I am grateful to the Canterbury Branch of the Royal Society of New Zealand for a grant supporting my travel and presentation at an overseas conference during my thesis work. Thank you also to my friends for their encouragement of my studies, and for reminding me on occasion that a world exists outside of academic research. Finally, a huge thank you to my parents for their never ending support of my endeavours.

Abstract

Ischaemic heart disease (IHD) is the most common cardiovascular disease, and is a major cause of mortality globally. The underlying process of IHD involves the development of atherosclerotic plaques on the arterial wall. These plaques can subsequently rupture and release thrombogenic species into circulation, or can occlude the vessel downstream following detachment. Such complications result in ischaemia—a restriction of blood supply to tissue that results in a shortage of vital cellular nutrients, such as oxygen and glucose. Recent publications hypothesise that cellular ionised calcium (Ca^{2+}) concentrations play an important role in atherogenesis.

There has been a significant amount of research on cardiovascular disease within multiple sub areas, including: *in vivo* and *in vitro* experimental work, computational fluid dynamics (CFD) simulations, and computational modelling of pathological behaviour. However, a combination of these fields will provide a greater understanding of the conditions that promote plaque development.

The research presented in this thesis consists primarily of massively parallel simulations of arterial bifurcations which used CFD to generate the input agonist maps for each arterial mesh. Micro-scale dynamics of coupled endothelial cells (ECs) and smooth muscle cells (SMCs) were modelled in bifurcation surfaces containing over one million cells. In particular, the effect bifurcation angulation may have on atherosclerosis development was investigated. A number of improvements were introduced to the original coupled cells model to perform these simulations.

A surface-mesh generation pipeline capable of creating geometrically varying 3-D surfaces, including EC and SMC layers, was implemented. These surfaces were used in CFD simulations to generate agonist input maps, and to define the EC and SMC layers on which the dynamics in our simulations are mapped. A detailed inositol triphosphate (IP_3) pathway and gap-junction currents were introduced to the coupled cells model. These additions were to ensure our simulations present physiologically accurate results when compared to related experimental research and computational modelling. Finally, the parallel implementation that enabled our simulations to be conducted at the macro scale was improved by the introduction of Open-Multi-Processing (OpenMP).

The massively parallel simulations displayed propagating Ca^{2+} waves in SMCs and steady-state concentrations of Ca^{2+} in ECs. Particularly complex SMC Ca^{2+} behaviour was observed in the lateral regions where the main stem meets the branches. Waves propagated in a slower, sporadic manner, and over significantly shorter distances. Further, we observed lower time-averaged Ca^{2+} concentrations in arterial geometries with wider bifurcation angles compared to those with narrower bifurcation angles.

The regions of low EC and SMC Ca^{2+} concentrations correspond to the sites research utilising CFD agrees are those most likely to experience plaque development due to flow detachment. Furthermore, we noted the low Ca^{2+} concentrations in these areas are more prominent in arterial geometries with wider bifurcation angles. These results suggest bifurcation angulation may have a signifcant effect on the susceptibility of arterial regions to atherosclerosis development.

Abbreviations

API application programming interface

ATP adenosine triphosphate

Ca^{2+} ionised calcium

CFD computational fluid dynamics

cGMP cyclic guanosine monophosphate

CICR calcium-induced calcium release

Cl^{-} ionised chloride

EC endothelial cell

ER endoplasmic reticulum

FSI fluid-structure interaction

GPCR G-protein-coupled receptors

IHD ischaemic heart disease

IP_3 inositol triphosphate

K^{+} ionised potassium

LCA left coronary artery

LDL low-density lipoprotein

MPI message passing interface

MRI magnetic resonance imaging

MUSCL Monotonic Upstream-Centred Scheme for Conservation Laws

Na^{+} ionised sodium

NO nitric oxide

ODE ordinary differential equation

OpenMP Open-Multi-Processing

OSI oscillating shear index

PIP_2 phosphatidylinositol 4,5-bisphosphate

PLC phospholipase C

PMCA plasma membrane Ca^{2+}-ATPase

RRT relative resident time

SERCA sarco/endoplasmic reticulum Ca^{2+}-ATPase

SIMPLE Semi-Implicit Method for Pressure-Linked Equations

SMC smooth muscle cell

SR sarcoplasmic reticulum

TAU Tuning and Analysis Utilities

TAWSS time-averaged wall shear stress

transWSS transverse wall shear stress

VOCC voltage-operated calcium channel

VPH Virtual Physiological Human

VTK Visualisation Toolkit

WSS wall shear stress

Chapter 1

Introduction

Cardiovascular diseases are a group of disorders specific to the heart and blood vessels. Ischaemic heart disease (IHD) is the most common cardiovascular disease, and is the leading cause of death globally (World Health Organisation, 2015). The underlying process of IHD involves the formation of atherosclerotic plaques in coronary arteries (Mendis et al., 2011), which can result in heart failure (National Heart Lung and Blood Institute, 2016).

Atherosclerotic lesion progression begins as regions on the inner-most arterial layer—the endothelium—undergo inflammatory activation, resulting in increased production of leukocyte adhesion molecules. These adhesion molecules allow blood-borne monocytes to more readily bind to the endothelium, whereas under normal conditions prolonged contact is resisted (Libby, 2002).

There are many complications that can follow atherosclerotic lesion formation. They include full vessel occlusion during plaque growth, and plaque rupture. Upon rupturing, thrombogenic materials are released into circulation and can induce thrombus (clot) formation in the lumen. These clots can occlude arteries outright or can travel downstream and occlude smaller branches. In all cases of occlusion, insufficient blood supply downstream results in ischaemia (Libby, 2002).

Arterial Physiology

The arterial wall consists of three primary layers of tissue: *tunica intima*, *tunica media*, and *tunica adventitia*. The intima consists of a single layer of endothelial cells (ECs), the media consists of one or many layers of smooth muscle cells (SMCs), and the adventitia is made up of connective tissue (Figure 1.1). Both ECs and SMCs are typical eukaryotic cells; they contain membrane bound organelles such as the cell nucleus, and are surrounded by a phospholipid bi-layer cell membrane. The liquid matrix surrounding the organelles is called the cytosol, and consists largely of water and ionic species, such as ionised calcium (Ca^{2+}), ionised potassium (K^{+}), and ionised sodium (Na^{+}).

ECs typically align axially, with the flow of blood, whilst SMCs attempt to align circumferentially. These orientations reflect the cells' respective physiological roles. The

endothelial layer acts as a mediator in the transfer of chemical species to and from the surrounding tissue, and individual ECs therefore have relatively large surface areas to which molecules and ions in the circulatory system can bind. Conversely, SMCs relax or contract in response to different stimuli to regulate blood flow, and wrap circumferentially around the intima. These cyclic dilations and contractions are known as vasomotion, and are mediated by Ca^{2+}-initiated formation of crossbridges between myosin and actin filaments (Hai and Murphy, 1988).

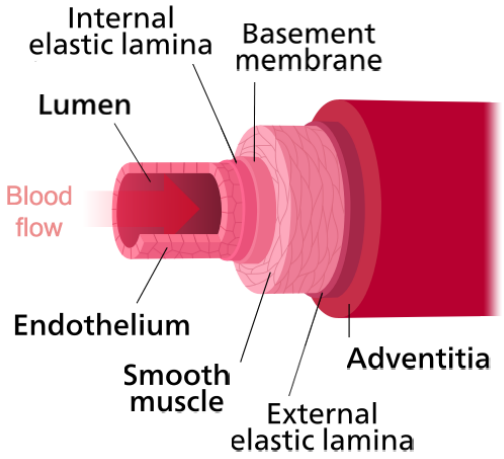

Figure 1.1: Labelled diagram of an artery, including the different layers of tissue. Adapted from: Kelvinsong - Own work, CC BY-SA 3.0, `https://commons.wikimedia.org/w/index.php?curid=25179416`.

The endothelium and smooth muscle layers are not isolated from one another—chemical species are able to diffuse between them through cellular communication channels. These channels are known as gap junctions. They are composed of connexin protein subunits and allow direct intercellular communication. The Cx37 homotypic connexins are highly selective and allow only the transfer of monovalent cationic currents; they have the most influence on the membrane potential (Rackauskas et al., 2007). The Cx40 connexin protein subunit favours divalent cations, and is therefore the major contributor to gradient-driven Ca^{2+} concentration currents. The Cx43 connexin is the least selective and allows the passage of a range of large and small molecules, such as adenosine triphosphate (ATP) and inositol triphosphate (IP_3) (Bedner et al., 2006).

1.1 Research Objective

The preferential locations of atherosclerotic plaque development are strongly associated with regions of disturbed haemodynamics, such as flow detachment surrounding bifurcations. Consequently, arterial geometry is likely influential in determining the sites of plaque growth within the vasculature. The literature has not yet provided a full explanation of the connection between arterial geometry and the localisation of atherosclerotic plaque formation.

The research presented in this thesis investigates whether variations in arterial bifurcation geometry can influence the development of atherosclerosis or otherwise affect local susceptibility to plaque formation. This investigation utilises massively parallel simulations of coupled arterial cells, with physiologically accurate input agonist maps derived from computational fluid dynamics (CFD) simulations, to examine how bifurcation angulation can affect the behaviour of coupled cells. Micro-scale dynamics in ECs and SMCs are modelled on arterial bifurcation surfaces containing approximately one million cells. The chemical species within individual cells, and the coupling between them, are described for physiological fidelity. However, atherosclerotic plaques have characteristic length scales much larger than a single cell in the arterial wall. The macro-scale phenomena are therefore studied in conjunction with the micro-scale.

1.2 Thesis Overview

- The literature review presented in Chapter 2 provides context to this research and highlights the importance of using a multi-scale simulation tool in the investigation of pathological conditions.
- The methods used to perform physiologically accurate simulations of arterial bifurcations are presented in Chapter 3. They include: the generation of arterial surface meshes and input agonist maps, the underlying mathematical cellular model, and the parallel implementation which enables simulations to be performed on a macro-scale.
- Chapter 4 presents the results of the macro-scale simulations and the extensions to their various components.
- Chapter 5 contains a discussion of the results in Chapter 4 and conclusions. It considers limitations of the current work and suggestions for future work.
- The Appendices contain the details of the coupled cells model, including definitions of all fluxes and model parameters, and also list outputs (to date) from the research presented in this thesis.

Chapter 2

Literature Review

This chapter gives context to the research presented in later sections by reviewing selected publications related to pathological changes in arterial physiology, with an emphasis on those seeking to define the conditions conducive to the development of atherosclerosis. In addition, it suggests why research in this field has not yet been able to describe precisely how vascular geometry contributes to atherosclerosis development, with regard to emergent properties of cellular behaviour on micro and macro scales. Three domains of related research are considered: localised disruptions of blood flow in arterial geometries, the effects these disturbances can have on cellular dynamics, and the development and use of computational physiological models of varying scales.

2.1 Flow Metrics

Local haemodynamics are important in all stages of atherosclerosis, from its early development through to determining the fate of more mature plaques. One of these dynamics, wall shear stress (WSS), has a special significance. WSS is a measure of the mechanical force at the luminal boundary layer due to the flow of blood. This layer is in constant contact with the endothelium, and as such plays a large role in determining the rate of absorption of blood-borne molecules by endothelial cells. There are many related measures, such as time-averaged wall shear stress (TAWSS), transverse wall shear stress (transWSS), oscillating shear index (OSI), and relative resident time (RRT). TAWSS describes the averaged WSS over a given period, typically a cardiac cycle. TransWSS is the averaged WSS components over a cardiac cycle perpendicular to the temporal-mean WSS vector. OSI highlights areas where WSS presents directional changes, and RRT evaluates the length of time molecules stay near a section of the vessel wall. These metrics play pivotal roles in assessing both the likely locations of lesion development, and the risks of deterioration and rupture in mature plaques.

In a recent paper, Pinto and Campos (2016) described a numerical study of these flow metrics, and their application in the left coronary artery (LCA). Using patient-specific LCA geometries, they constructed their own idealised geometries and ran multiple simulations

using CFD to ascertain the importance of each descriptor when compared to known areas of plaque development.

In agreement with studies looking at known locations of lesion development, their simulations displayed low values of TAWSS and high values of both RRTs and OSIs around the neck of the bifurcation. However, they noted that OSI was less important than the other metrics. See Figure 2.1 for both TAWSS and RRT values over presented simulations. They concluded that both TAWSS and RRT metrics are highly important when considering the locations of atheroma development.

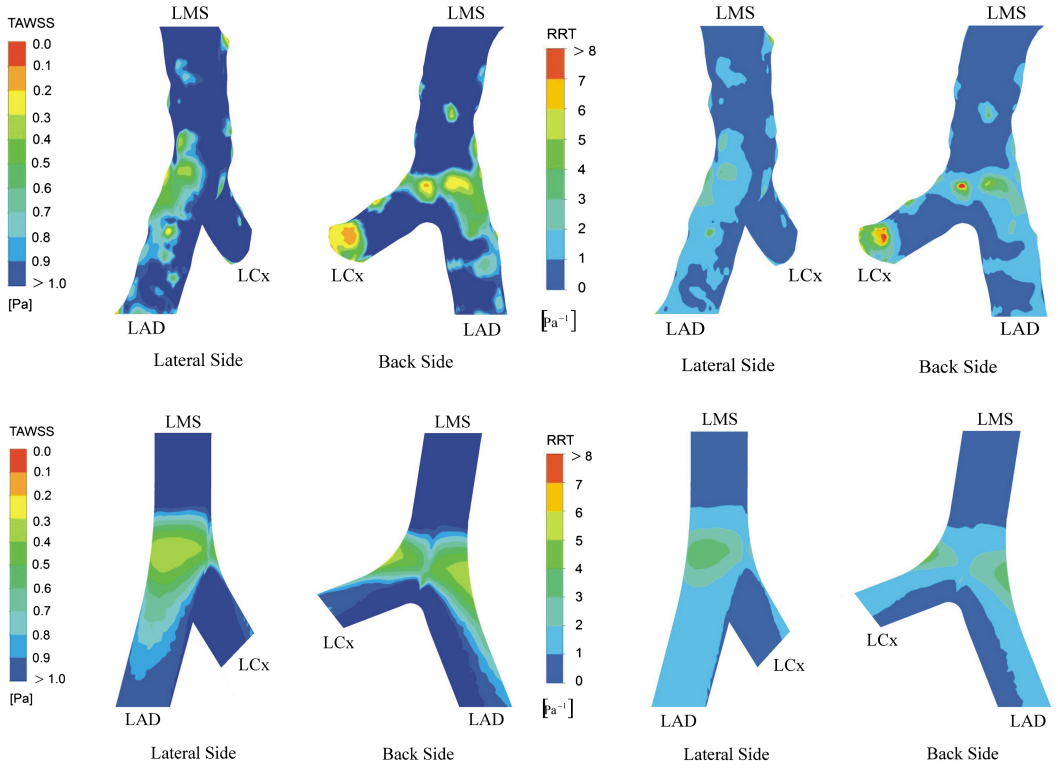

(a) Time-averaged wall shear stress.

(b) Relative resident time.

Figure 2.1: Flow metrics for both patient-specific (top) and idealised-model (bottom) geometries during CFD simulations. Both from Pinto and Campos (2016), with permission.

Longest et al. (2003) conducted a study on near-wall RRT for monocytes, and came to a similar conclusion as to the importance of this descriptor. They found a significant positive relationship between observed monocyte deposition locations and RRTs. Indeed, the current consensus is that low WSS and high RRT/OSI are the initiation mechanisms of atherosclerosis (Wentzel et al., 2012). This has not always been apparent. Fry (1969) conducted a set of experiments to quantify physiological responses of the arterial intima to a variety of mechanical stresses, and concluded that high WSS values are responsible for endothelial damage and subsequent pathological responses. Recent publications have found the opposite to be true (Wentzel et al., 2012; Cecchi et al., 2011), and Caro et al. (2012) noted peak WSSs required to damage the endothelium were far greater than those found normally in the arterial system—even at high flow rates during exercise.

Warboys et al. (2010) found acute and chronic exposures of WSS have opposite effects on the permeability of endothelial cells to macromolecules. With this in mind, some conclusions made by Fry (1969) may be able to co-exist with the established correlation between low WSS/high OSI and atherosclerosis. Under acute (but not chronic) shear stress conditions, an enhanced permeability of monocytes—whose involvement in early atherosclerotic lesion development is well known (Libby, 2002)—may very well result in the onset of atheroma.

Mohamied et al. (2016) presented a study on arterial blood flow using the recently-introduced metric transWSS. In particular, the authors investigated the sensitivity of transWSS to both aortic geometry and inflow waveform. Time-dependent CFD simulations were performed using geometries of immature rabbit thoracic aortas to analyse the components of transWSS. They found transWSS was insensitive to inflow waveform, but was sensitive to geometric variations, such as torsion, taper, and curvature of the arch and proximal descending aorta. This flow metric may be highly important in future research focused on the prediction of atherogenesis; Mohamied et al. (2016) noted transWSS correlated strongly with the appearance of fatty streaks surrounding aortic ostia.

2.2 Effects of Variation In Bifurcation Geometry

Based on the observation that atherosclerotic plaques tend to develop in regions near bifurcations or subject to curvature, it is now widely established that haemodynamic forces play important roles in the development and progression of atherosclerosis (Malek et al., 1999). Areas of detached flow can result in the disruption of vascular homoeostasis, which in turn may lead to endothelial dysfunction, and the development of atherosclerotic plaques (Lerman and Zeiher, 2005). It is therefore prudent to learn exactly how variations in these particular geometries might affect local haemodynamics.

With this objective, Lee et al. (2008) conducted a number of CFD simulations on carotid bifurcation geometries, derived from magnetic resonance imaging (MRI) of many young adults. They found significant relationships between disturbed flow and both proximal area ratio and bifurcation tortuosity, but not bifurcation angle, planarity, or distal area ratio.

In related research, Dong et al. (2014) reported a set of experiments simulating fluid-structure interaction (FSI) within a set of varying coronary bifurcations. Simulations were situated between the left anterior descending (LAD) and left circumflex (LCX) arteries, where the bifurcation angle ranges from 60° to 100°. The aim was to elucidate the links between coronary artery branch angulation, local mechanical forces, and haemodynamics surrounding bifurcation points. Figure 2.2 depicts the parameters for simulation geometries.

In contrast to Lee et al. (2008), Dong et al. (2014) found the wider angles, specifically the LCX-side bifurcation shoulder, were the most likely sites of disturbed flow. This included low WSS and high OSI values over the entire cardiac cycle. Further, Dong et al. (2014) suggested there is a strong correlation between bifurcation angle and atheroma development.

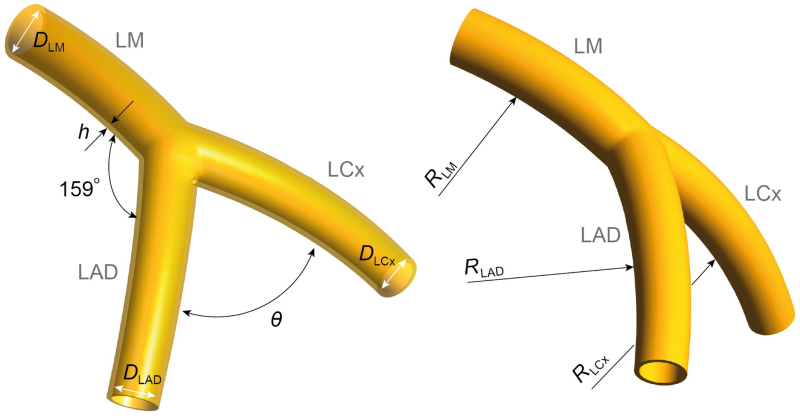

Figure 2.2: Idealised arterial bifurcation geometry. h indicates vessel wall thickness, D stands for vessel diameter and R for branch curvature. Taken from Dong et al. (2014), with permission.

One possible explanation for this discrepancy is a difference in assumptions. As in some other research attempting to correlate the location of disturbed flow with variation in geometry, the simulations reported by Lee et al. (2008) assumed a rigid arterial wall. However, this neglects the known elasticity of the wall. By running FSI, Dong et al. (2014) were able to model both blood flow and arterial wall deformation. These opposing conclusions result in the relationship between variation in bifurcation angulation and vascular disease being unclear. With the goal of elucidating this relationship, research presented in later chapters has incorporated variable bifurcation geometries with macro-scale simulations of EC and SMC behaviour.

2.3 Lipid and Liposome Modelling

Low-density lipoprotein (LDL) is one of the five major groups of lipoprotein. Lipoproteins are responsible for transferring lipids around the body, and consisted of many different proteins themselves. However, they pose a risk in the development of atherosclerosis after invading the endothelium; higher concentrations of LDL are strongly linked to increased accumulation of atherosclerotic plaques over time (Seymour et al., 1987). Once penetrating the endothelium, LDL are able to form lipid packets, named liposomes, which in turn can be devoured by invading monocytes in the process of becoming foam cells.

It has been shown that cellular level 'leakage' can occur, resulting in significant transendothelial transport of LDL. Yin et al. (1997) hypothesised that the LDL from such leaks become those found in liposomes, and that these liposomes show formation and growth resembling classic polymerisation processes. Using experimental data on liposome size, from rabbits both chronically hypercholesterolemic (WHHL) and those fed a high-cholesterol diet, Yin et al. (1997) created a number of models for the accumulation and growth of liposomes in the arterial intima. Even the simplest of these models agreed with the WHHL data, and when combined with slow transendothelial leakage also accounted for the cholesterol-fed rabbit data.

The main limitation of this work was simply the paucity of data on which the model was based and validated against. Generating histograms of liposome accumulation and size in the endothelium is difficult; the data were derived from a small area of the aorta, and from a small number of specimens (2 WHHL and 3 cholesterol-fed rabbits).

Tying this model after further validation to that of a macro-scale cellular model of particular areas in the vasculature would provide a significant step forward. Further, if factors pertaining to the rate of cellular leakage were modelled, a solid link between cellular behaviour and the accumulation of lipids in atheroprone areas could be made.

2.4 Intimal Thickening

The thickness of the arterial intima, in particular the spatial and temporal changing of thickness, can be used as a marker for atherosclerosis. de Groot (2004) estimated atherosclerosis progression from early childhood into old age by measurement of intimal thickness in subjects with familial hypercholesterolemia. They found, by comparison to a healthy control group, the thickness of the intima could be used as a predictor for atherosclerosis. However, this conclusion was specific to the particular disease being studied, and should not necessarily be applied more widely.

Lee and Chiu (1992) conducted a number of numerical simulations on both smooth and curved vessel segments to correlate wall shear rate, geometry, and the localisation of lesions. They introduced a model of dynamic intima thickening into these simulations, in which three meshes were used: a straight artery with a stenosis, a 90° curved smooth artery, and a 90° curved artery with a stenosis. These stenoses protrude in one direction (circumferentially non-uniform) from within the vessel, replicating the nature of an atherosclerotic plaque. However, simulations involving arterial bifurcations were not included in the study. This now appears important, given the known tendency for lesions to develop in the vicinity of bifurcations.

Stenoses resulted in areas of greater intima thickening in all simulations that were run, both at the stenosis and a small distance directly downstream. Further downstream, the effects of the stenosis vanished and the behaviour of the geometry resumed—straight vessels had uniform intima thickness, while curved ones had thicker inner walls and thinner outer walls. These locations are consistent with those at which atherosclerotic plaques are known to develop (Asakura and Karino, 1990; Malek et al., 1999).

Wall thickness as a metric may be highly important for determining different locations of plaque formation, but it should co-exist with a number of other measured variables. For example, when combined with a macro-scale model of cellular behaviour in ECs and SMCs, it will likely prove to be much more informative. Monocytes will only attach to ECs if those ECs are susceptible, and this may be a function of ionic dynamics in the intima. Linking changes in intima thickness over time, and the resulting differences in measures such as WSS to the behaviour of chemical species on a cell-by-cell basis may result in a more powerful predictive tool.

2.5 Computational Modelling of Arterial Physiology

The research reviewed in Sections 2.1 and 2.2 has focused on the modelling of blood flow and its effect on arterial physiology. Commonly, CFD simulations have been used to do this. This section considers the literature on cellular modeling, that is, observing the behaviour of chemical species in single and coupled cells. It is important to understand what previous models have revealed, and how they compare to the models developed in this thesis.

2.5.1 Coupled EC/SMC Dynamics

Koenigsberger et al. (2004) presented a detailed model of cellular dynamics, focusing on the generation and synchronisation of Ca2+ oscillations in a population of coupled SMCs. They extended a previous mathematical model provided by Parthimos et al. (1999) to describe five state variables with ordinary differential equations (ODEs) in each SMC: cytosolic calcium concentration, sarcoplasmic reticulum (SR) calcium concentration, membrane potential, cytosolic IP_3 concentration, and the open state probability of the calcium-activated potassium channels for the SMC layer.

Koenigsberger et al. (2004) developed this cellular model in order to research the conditions affecting Ca^{2+} oscillations in populations of SMCs. They found gap junctional coupling of Ca^{2+} was necessary for the synchronisation of Ca^{2+} oscillations, that electrical coupling was able to both generate and desynchronise Ca^{2+} oscillations, and that IP_3 diffusion did not appear to play a large role.

Koenigsberger et al. (2005) then investigated the role of the endothelium in arterial vasomotion, noting that the understanding of its importance was unclear. They therefore modified their model to include a population of ECs, coupled both homocellularly with one another, and heterocellularly to adjacent SMCs. To describe the dynamics of a single EC, equations from Goldbeter et al. (1990) were adapted. Those variables were cytosolic calcium concentration, endoplasmic reticulum (ER) calcium concentration, membrane potential, and cytosolic IP_3 concentration. A visualisation of the cell population and coupling used in simulations is shown in Figure 2.3.

This model provides the basis of the research presented in this thesis; the equations and parameters are described in more detail in Section 3.3 and Appendix A.

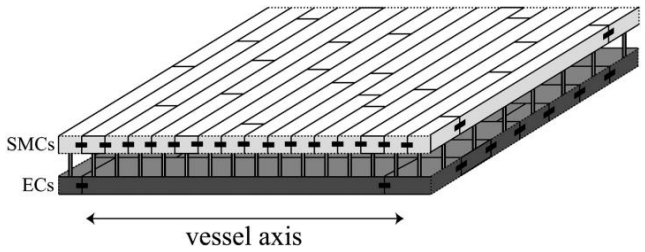

Figure 2.3: Geometry and communication for coupled EC and SMC layers. Homocellular connections are depicted with solid dashes (-), while heterocellular connections with double lines (‖). From Koenigsberger et al. (2005), with permission.

2.5.2 Macro-scale Modelling

The coupled EC/SMC model of Koenigsberger et al. (2005) provided an excellent basis for cellular modelling on a micro-scale. Shaikh et al. (2012) adapted this, and studied the onset and development of atherosclerotic plaques in the vasculature. However, plaques have characteristic lengths much greater than a single cell. To learn more about this disease, it was necessary to examine macro-scale phenomena. Given that Koenigsberger et al. (2005) considered populations of approximately 60 SMCs and 30 ECs, significant modifications and additions were necessary to examine emergent behaviour on the desired scale. These modifications marked the beginning of the Coupled Cells project (Shaikh, 2011).

The Coupled Cells model was able to simulate arterial segments—populations of millions of coupled ECs and SMCs—by decomposing those populations into blocks of cells, and using the message passing interface (MPI)[1] library for communication between blocks. With this technique, simulations could be parallelised and run on supercomputing platforms; this was necessary because simulations of this order would be computationally infeasible if run serially.

This scale allowed for the simulation of flow separation, a phenomenon that spans a relatively large populations of cells, by generating a lumenal agnostic input map that followed a non-uniform gradient. This gradient was such that the ECs experienced a steep change in lumenal ATP concentration in approximately the middle third of the artery segment, and an almost uniform concentration at its extremities.

Multiple coupling cases were introduced, each with varying coefficients seen in both homo- and heterocellular coupling equations. These coupling cases simulate various conditions, both normal and pathological in nature. Simulations with each of the four coupling cases exhibited different Ca^{2+} dynamics, most notably the fourth, which displayed an increased global cytosolic concentration due to the lack of hyperpolarisation from ECs (due to severely weakened heterocellular communication).

Shaikh et al. (2012) provided an excellent analysis of the conditions surrounding atherogenesis using a newly developed massively parallel coupled cells model. However, this disease is highly complicated, and still not fully understood, and further research is required.

2.5.3 ATP to IP_3 Pathway

Plank et al. (2006) proposed low Ca^{2+} concentrations in ECs may contribute to the onset of vascular disease. Further, Malek et al. (1999) and Chen and Popel (2007) demonstrated that the production of nitric oxide (NO) is reduced in areas of low WSS, which in turn leads to endothelial dysfunction (Davignon and Ganz, 2004) resulting in an increased probability of atherosclerotic plaque formation. The production of NO is a function of Ca^{2+} concentration. Cytosolic Ca^{2+} release in ECs is largely controlled by IP_3, which is produced in the ATP to IP_3 pathway.

The work of Lemon et al. (2003) provided a mathematical account of IP_3 and Ca^{2+} dynamics in a single cell, following metabotropic receptor activation by an external agonist

[1] `http://mpi-forum.org/`

concentration. They detailed both the phosphorylation, uncoupling of G-protein, dephosphorylation, and recycling of metabotropic receptors, as well as the G-protein cascade. This included the activation of G-protein and PLC, the subsequent hydrolysis of phosphatidylinositol 4,5-bisphosphate (PIP_2) to IP_3 and DAG, and the replenishment of PIP_2 in the cytosol. Their results showed the importance of explicitly modelling both the PIP_2 and metabotropic receptor recycling for maintaining IP_3 and Ca^{2+} concentrations over sustained applications of agonist.

In contrast to this detailed modelling, Koenigsberger et al. (2005) assumed a linear relationship between ATP and IP_3 concentrations and neglected intermediate processes. Given the research presented in this thesis builds upon a framework in which the Koenigsberger et al. (2005) model is included, a more detailed review of this assumption is necessary. This is given in Section 3.3.3.

2.5.4 SMC Synchronisation

A model of SMC synchronisation, in particular Ca^{2+} dynamics in a population of 14 SMCs, was presented in Jacobsen et al. (2007). This work was very similar to that of Koenigsberger et al. (2004), although it contained two distinguishing features.

First, Jacobsen et al. (2007) modelled cyclic guanosine monophosphate (cGMP) concentration within a small population of SMCs, and the effects it had on intercellular synchronisation. They reported that low concentrations results in unsynchronised waves of Ca^{2+} across their population of cells, while high concentrations could initiate sustained vasomotion.

Second, Jacobsen et al. (2007) described the existence of gap-junction currents due to both membrane potential and concentration gradients of ionic species between neighbouring cells. In contrast, Koenigsberger et al. (2004) diffused membrane potential as if it were another ion or molecule, which now appears physiologically incorrect. This simplification will also be addressed in Section 3.3.3.

2.5.5 Arterial Vasomotion and Vascular Disease

Boileau et al. (2015) provided a computational framework of cellular behaviour over large vessel segments, not dissimilar to that of Shaikh et al. (2012), with an emphasis on realistic arterial geometries generated from patient data. The model was designed to study arterial vasomotion and possible links it might have to vascular disease. This is highly relevant to the research presented in later chapters of this thesis.

The simulations conducted by Boileau et al. (2015) used one 3-dimensional vessel segment, specifically of the carotid artery. The input for each simulation was an influx of Ca^{2+} into SMCs via nonspecific cation channels. As the intercellular Ca^{2+} coupling was increased, sporadic oscillatory activity transformed into Ca^{2+} wavefront propagation along the entire vessel.

Boileau et al. (2015) included homocellular coupling between SMCs in their model;

however, heterocellular coupling between SMCs and ECs was not included. It is well known that endothelial dysfunction can lead to vascular disease (Davignon and Ganz, 2004; Libby, 2002), and incorporating communication between ECs and SMCs is therefore crucial if a connection between arterial vasomotion and vascular disease is to be made.

The simulations presented in Boileau et al. (2015) did not use physiologically accurate agonist input, and consequently did not consider the effect of blood flow within their particular geometry. Further, the authors conducted simulations on a single arterial surface mesh. In contrast, the research presented in this thesis will use multiple surface meshes with varying geometric properties, and physiologically accurate agonist maps for each.

2.6 Summary

An overview of related published works has been detailed in this literature review to provide context for the research presented in later chapters. In particular, flow modelling in various arterial geometries, the effect disruptions to flow can have on arterial dynamics, and the development of mathematical models that describe varying scales of physiology are examined.

Many flow metrics have been used to highlight regions within arterial geometries that experience flow detachment. Pinto and Campos (2016) stated TAWSS and RRT are particularly important measures when describing flow detachment in arterial bifurcations, while Dong et al. (2014) concluded wider bifurcations are subject to greater flow detachment, and may be more likely to develop atherosclerotic lesions. Simultaneously, many computational models of cellular dynamics have been implemented, such as that of Koenigsberger et al. (2005). They presented a model of coupled EC and SMC over relatively small sections of the arterial wall, and were able to demonstrate vasomotion through the introduction of an agonist to endothelial receptors.

Little research has utilised the results from various flow metrics in conjunction with physiological simulations. Fewer still perform their simulations at an appropriate scale, considering the characteristic size of atherosclerotic plaques. Mechanisms of plaque formation must be studied over considerable distances, such as hundreds to thousands of cell lengths. The research presented in this thesis makes use of a detailed micro-scale coupled cells model, able to demonstrate time-dependent dynamics for numerous chemical species, in simulations of varying arterial geometries containing upwards of one million cells. The effects of vessel bifurcation angulation on plaque formation is studied using this sophisticated model, which incorporates a number of improvements over earlier models. Importantly, the development of this platform also provides opportunities for further research in this field.

Chapter 3

Methods

The methods for investigating the connection between atherosclerosis development and arterial geometries are presented in this chapter. Some of these tools were created as a part of this work, while others were developed as extensions to previous work. The description of these tools will reveal details of the key components of our massively parallel physiological simulations; these include the generation of arterial surface-meshes and input agonist maps, the underlying mathematical coupled cells model, and the parallel implementation which enables macro-scale simulations.

3.1 Arterial Surface Meshes

Surface meshes are required to conduct physiological simulations of corresponding three-dimensional arterial segments. These surfaces are used as input for CFD simulations to create input agonist maps. Furthermore, the surfaces define the EC and SMC layers on which the dynamics of cellular species presented in the simulations can be mapped.

A flexible method of creating surface-meshes of arterial segments with varying geometries and scales is presented below. This method has been implemented as a pipeline of modular functionality. A number of differently angled bifurcation surfaces that utilise this pipeline are then introduced, the geometries of which served as the core surface-meshes for the macro-scale physiological simulations presented in Chapter 4.

3.1.1 Mesh Generation Pipeline

The process of mesh generation was designed as a series of filters using the Visualisation Toolkit (VTK) library. These filters are connected to one another to create a pipeline—a multi-stage process beginning with the partitioning of an input centreline and ending with the output of 3-D EC and SMC layers. The key stages of the pathway are outlined below.

Centreline Generation

In the context of medical image analysis, centrelines are sequences of points following the centre of a vessel, with associated radius values at each point. Anatomical centrelines can be obtained from patient data, typically using cardiac computed tomography imaging. To create surfaces with specific geometric properties, such as varying bifurcation angles, a method of creating synthetic centrelines was implemented. This implementation provided a large amount of control over the complexity of generated centrelines. For example, the number of branches and their locations, the vessel radii along each branch, and curvature are all controllable using various input parameters. Figure 3.1 provides an example of a non-planar branching centreline with decreasing radius values as a function of distance from the inlet.

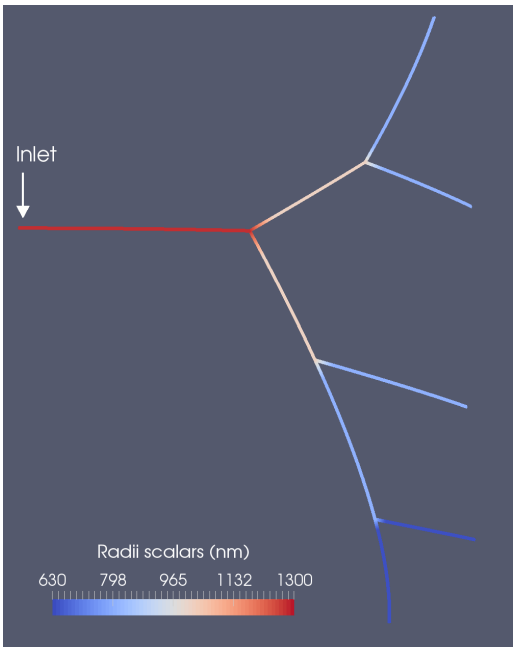

Figure 3.1: Branching centreline representing a subsection of a coronary tree, with corresponding decreasing radii moving down the branches. The inlet of the main stem is labelled.

Centreline Partitioning

Vessel centrelines are used as input into the pipeline of VTK filters, the first of which partitions the centreline into a number of smaller sections. This is necessary for the subsequent filter in the pipeline, which requires particular segment lengths as input as opposed to entire vessel skeletons.

There are two constraints for segments; first, they must not exceed some maximum length, and second, segments containing bifurcations must start some distance before the bifurcation point and end some distance after it on both branches. These constraints require this filter to be able to traverse the branches of a given centreline tree iteratively, and search ahead to detect/store locations of bifurcations to ensure no segments cause artefacts in later stages of the pipeline.

Surface Generation

The following technique provided by Bloor and Wilson (1989) has been implemented to create 3-D surfaces from the partitioned centreline segments. Each bifurcation can be decomposed into three semi-tubular surface segments by using the solution to a biharmonic equation. The biharmonic equation has the operator form given by

$$\left[\frac{\partial^2}{\partial u^2} + a^2\frac{\partial^2}{\partial v^2}\right]^2 \phi = f(u,v), \tag{3.1}$$

where ϕ is the space vector (x, y, z) and $f(u, v)$ can be either zero or an a priori defined function. For our geometries, u and v are orthogonal coordinates that provide axial and circumferential directions. The Neumann and Dirichlet boundary conditions for equation (3.1) define the rate at which the surface moves away from the boundary and its direction respectively.

Equation (3.1) is discretised into m (u direction) and n (v direction) points on the boundary. With this method the surface of each segment is unwrapped into a 2-D $m \times n$ grid in the u and v directions respectively. The solution now becomes a 2-D solution, rather than a 3-D solution. To obtain a complete 3-D surface, the semi-tubular segments can be joined together at the boundaries. A cloud of points is then collected from all joined surfaces. An implementation of a biharmonic equation solver in Fortran, freely available through online resources[1], was integrated into this filter.

Points to Mesh

The collection of points generated by the surface generation filter was used to create a mesh of planar quadrilaterals. An example of such a mesh with defined nomenclature is shown in Figure 3.2.

Subdivide Quadrilaterals

To create the EC and SMC layers, each quadrilateral in the surface-mesh was subdivided into cells. With the approximate physical dimensions of SMCs and ECs, 50×5 μm and 65×10 μm respectively, the SMCs and ECs are arranged into surface units where the area covered by 5 ECs corresponds to the area of 13 SMCs. The precise number of ECs and SMCs is parameterised. Figure 3.3 shows an example of ECs and SMCs arranged in two layers within a single quadrilateral on a bifurcation surface. All three surface-meshes were then written out in VTK's VTP format.

Outcomes

The modular approach presented here of generating arterial surface-meshes—a pipeline of independent and testable filters—provides a number of benefits.

[1] Bjorstad, P. E. (1980). Numerical Solution of the Biharmonic Equation. Retrieved from `http://http://www.netlib.no/netlib/bihar/dbihar.f`.

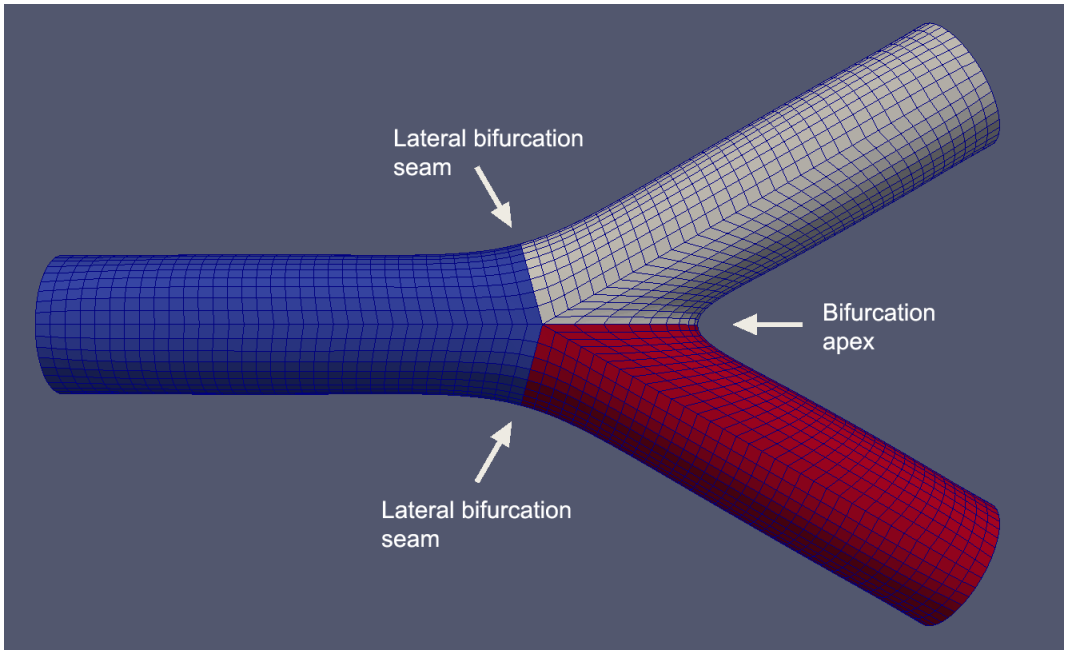

Figure 3.2: Quadrilateral decomposition of a bifurcating vessel segment where each branch is of 8.8 mm length and 2.6 mm diameter. The parent trunk is coloured blue, while the branches white and red. The bifurcation apex and lateral seams are labelled for later reference.

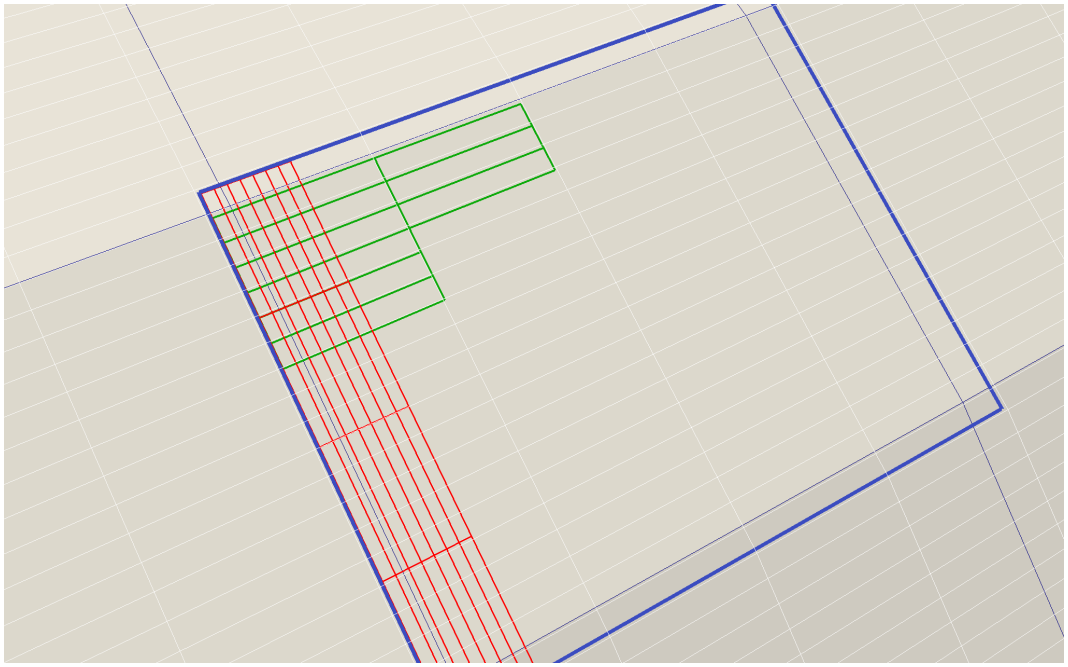

Figure 3.3: A quadrilateral mesh element showing the mutually orthogonal alignment of the ECs (green border) and the SMCs (red border) after its subdivision.

- It allows for the simple addition of new filters as more complex surfaces are required, and the ability to upgrade or replace existing filters as improvements are discovered. Furthermore, it is more understandable and modifiable by others who were not involved with its creation.

- Substituting more complex centrelines as input into the pipeline, such as the one shown in Figure 3.1, has allowed the development of more physiologically accurate vessel segments and tree structures. Figure 3.4 demonstrates this scalability.

Quadrilaterals surrounding the bifurcation seams vary in size as a result of the surface generation process. This is seen in Figure 3.2. Consequently, both SMCs and ECs vary in size too, given these layers are created as subdivisions of quadrilaterals. This is unintended and noted as a limitation to the surface generation pipeline. Further, the pipeline is currently better suited to the use of centrelines created synthetically. Those of real patients can be used too, but results are unpredictable. Sections of their centrelines may contain shape twists and turns that result in folds and other artefacts in the generated surfaces. We assume synthetic centrelines and the resulting surfaces are sufficiently complex for the experimentation presented in later chapters.

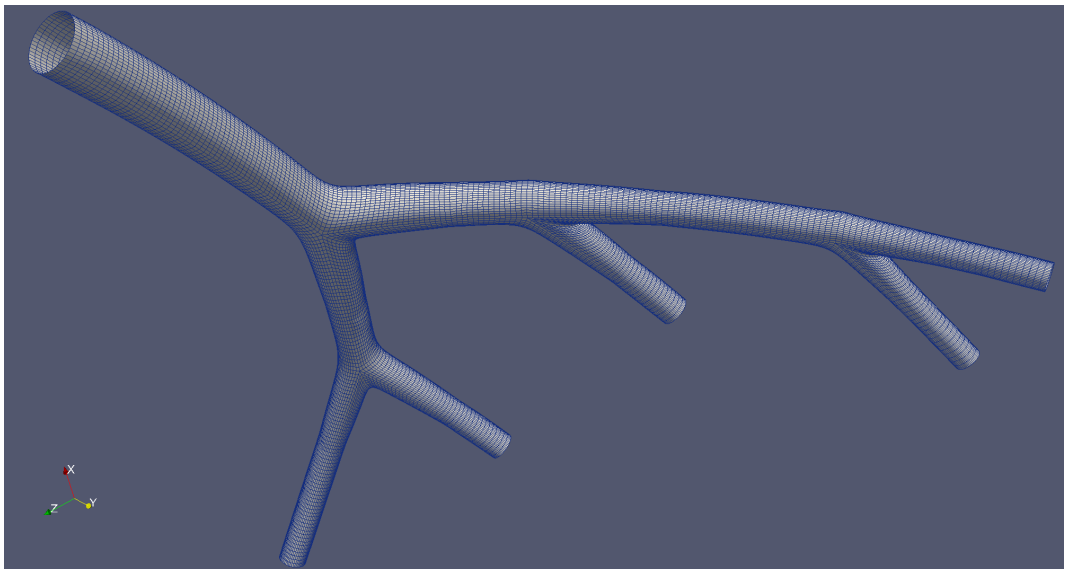

Figure 3.4: Surface mesh consisting of over 20,000 quadrilaterals spanning multiple branches. Slight curvature has been included to simulate a subsection of the coronary tree. Physiologically, this arterial tree would consist of millions of cells.

3.1.2 Varying Bifurcation Angles

The potential significance of varying arterial bifurcation geometry is highlighted in Section 2.2; these variations include tortuosity, ratio of proximal to distal areas, curvature, and angles between branches. In particular, bifurcation angulation appears to have a strong effect on flow behaviour in such a way that might correlate flow detachment with plaque development. This factor was therefore chosen as a subject of experimentation. Three different angles (measured between branches) were chosen within the range reported by Dong et al. (2014): 50°(symmetric bifurcation), 80°, and 110°. They were subsequently created using the mesh generation pipeline described above, and are shown in Figure 3.5. These surface-meshes contain two important properties other than the angle between branches. First, they are non-planar. While arterial curvature is not a subject of experimentation, the

vessels considered in this research belong to the coronary tree, which are naturally affected by curvature as they wrap around the ventricles of the heart. Second, the radii of the branches are different from that of the parent branch. They follow Murray's law, which relates the radii of downstream branches to a main stem. The formula is as follows:

$$r_p^3 = r_{d_1}^3 + r_{d_2}^3 + r_{d_3}^3 + \ldots + r_{d_n}^3 \tag{3.2}$$

where r_p is the radius of the parent branch, and r_1 through to r_n are the radii of the respective branches. The bifurcations used in this research contain two branches.

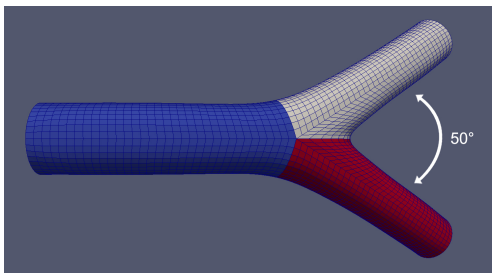

(a) Quadrilateral surface-mesh with a 50 degree bifurcation angle.

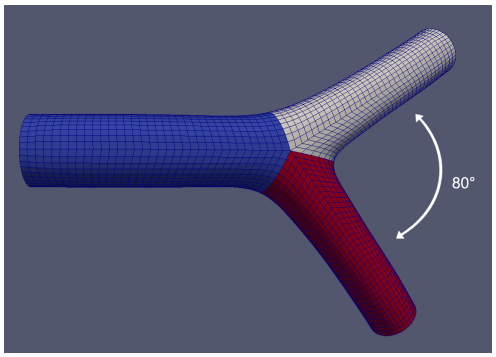

(b) Quadrilateral surface-mesh with an 80 degree bifurcation angle.

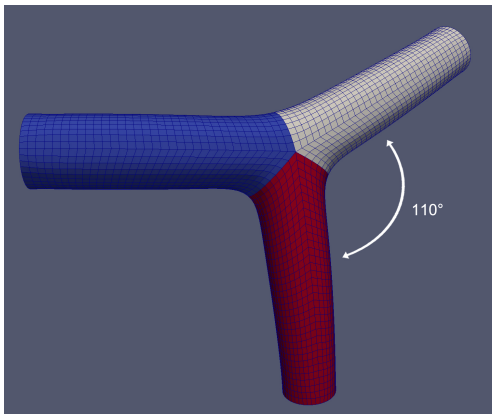

(c) Quadrilateral surface-mesh with a 110 degree bifurcation angle.

Figure 3.5: Three non-planar bifurcating quadrilateral surfaces with varying angles between branches. The main stem is blue, the left branch white, and the right branch red.

3.2 Agonist Map Generation

A great deal of complex cellular activity begins with the binding of agonistic molecules within the lumen to receptors on the endothelium. One such pathway is described later, in Section 3.3.1, which details binding of blood-borne ATP to ECs, and the resulting intra- and intercellular movement of chemical species in both ECs and SMCs. ATP is therefore used as an input stimulus in all simulations conducted in this research.

There are currently two variations of input; synthetically generated ATP maps, and time-averaged, physiologically accurate ones from CFD simulations that model the flow of blood and reaction of ATP with the endothelium. It is necessary for both synthetically and CFD generated input that the arterial surface-meshes are previously generated. Synthetic maps require geometry upon which to map ATP values, while the CFD simulations need a mesh in which to model flow and agonist binding.

3.2.1 Synthetic ATP Maps

Synthetic ATP maps were generated in order to highlight the fundamental patterns of the emergent macro-scale behaviour. These agonist maps are simpler than those generated with CFD simulations; they use non-planar variants of the surface-meshes described in Section 3.1, and show less complex spatial ATP concentration distributions. Arterial bifurcations for 60°, 80°, and 100°angle variations can be seen in Figure 3.6.

The agonist distribution pattern was chosen to approximate those patterns reported by Dong et al. (2014). The patches at the bifurcation apexes show increased ATP concentrations, while the patches near the lateral bifurcation seams show lower ATP concentrations, consistent with the areas of low WSS. As the angle of the bifurcation becomes wider, the patch by the near lateral bifurcation seam in Figure 3.6 shows lower values of ATP.

3.2.2 CFD Simulations

The generation of physiologically accurate input ATP maps was undertaken entirely by Dr. Stephen Moore, an expert in CFD based at the University of Melbourne, Australia. The simulations follow the algorithm described in the work of Comerford and David (2008), and use the open source CFD tool, OpenFOAM (Tabor et al., 1998). It is of vital importance to this research, and so is described below.

The flow field is solved iteratively via the continuity and momentum equations (3.3) and (3.4), on the assumption that the blood flow is steady state, incompressible, and of Newtonian rheology:

$$\nabla \cdot \mathbf{u} = 0 \tag{3.3}$$

$$\mathbf{u} \cdot \nabla \mathbf{u} = \nu \nabla^2 \mathbf{u} - \nabla p. \tag{3.4}$$

Here $\mathbf{u}$ represents the blood velocity vector field $\mathbf{u} = [u, v, w]$, p the kinematic pressure field, and ν the kinematic viscosity. The species mass transport was solved simultaneously via

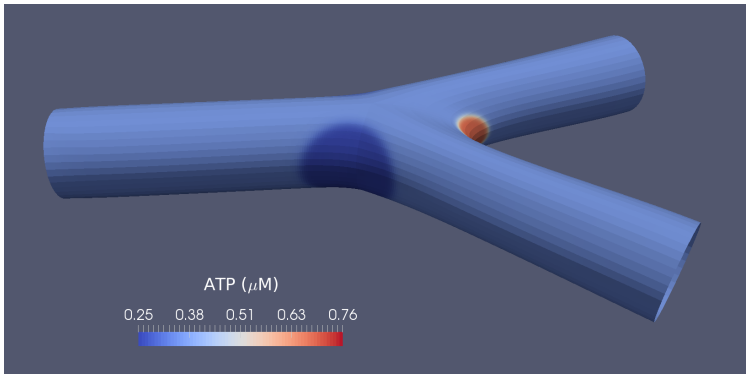

(a) 60° bifurcation angle.

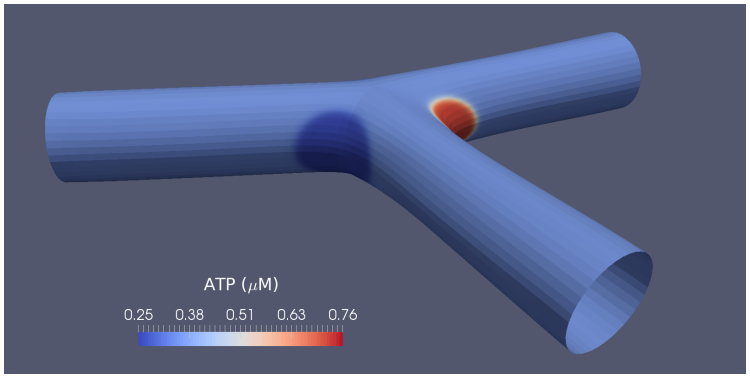

(b) 80° bifurcation angle.

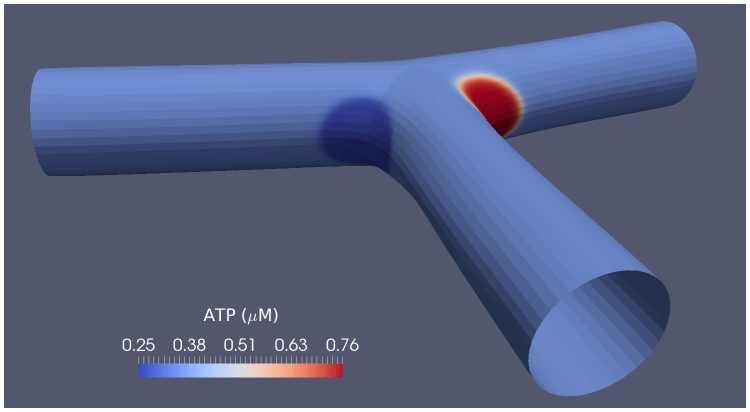

(c) 100° bifurcation angle.

Figure 3.6: Synthetic ATP maps for three arterial segments with 60°, 80°, and 100° angled bifurcations.

the conservation of species equation given by

$$\mathbf{u} \cdot \nabla \phi = D \nabla^2 \phi, \tag{3.5}$$

where ϕ is the species ATP concentration and D is the isotropic diffusion coefficient. The walls of the artery are assumed to be rigid and stationary. The governing equations were solved iteratively via the Semi-Implicit Method for Pressure-Linked Equations (SIMPLE) algorithm for pressure-velocity coupling; the convective terms were handled with second-order upwinding for momentum and third-order upwinding Monotonic Upstream-Centred

Scheme for Conservation Laws (MUSCL) scheme for chemical species.

A parabolic Dirichlet velocity profile was implemented on the inlet (the peak velocity was determined for the actual inlet area and the specified flow-rate) and zero velocity gradient Neumann boundary conditions on the outlets. The pressure field values were specified as zero-pressure gradient Neumann boundary conditions for the inlet and zero-pressure Dirichlet boundary condition on the outlets.

For the species boundary conditions a constant Dirichlet value of 1.0 μM was specified on the inlet and zero gradient Neumann boundary conditions on the outlets. Following Plank et al. (2006), the boundary condition was defined as follows:

$$D\frac{\partial\phi(x,0)}{\partial y} = K\phi(x,0) - S(x) \tag{3.6}$$

Here $S(x)$ represents the production of ATP as a function of WSS in the form of:

$$S(x) = S_0\Big(1 - exp\Big(-\frac{\tau_w(x)}{\tau_m}\Big)\Big)^3, \tag{3.7}$$

where the K and τ_m values were those reported by Plank et al. (2006). A reactive boundary condition is specified on the arterial walls; it is implemented iteratively by specifying a Neumann boundary condition for the ATP gradient, where the gradient itself is a function of ATP concentration. For each iteration the boundary condition is evaluated based on the current ATP concentration, then the ATP gradient is specified on the wall and the scalar transport equation is solved. The process is repeated until convergence is obtained.

All other parameters for mass transport were taken from Plank et al. (2006), and the wall shear stress was calculated from the Navier-Stokes flow-field.

CFD-Based Agonist Maps

Section 3.1.2 described the generation of arterial surface-meshes containing a variety of bifurcation angles. These surfaces provide not only the geometry in which the EC and SMC layers may be generated, but they also serve to define the surface of the boundary layers in the CFD simulations. The time-averaged agonist maps from these geometries can be seen in Figure 3.7. They display relatively high ATP concentrations at the bifurcation apex, low concentrations at the lateral bifurcation seams, and near uniform concentrations in all other regions.

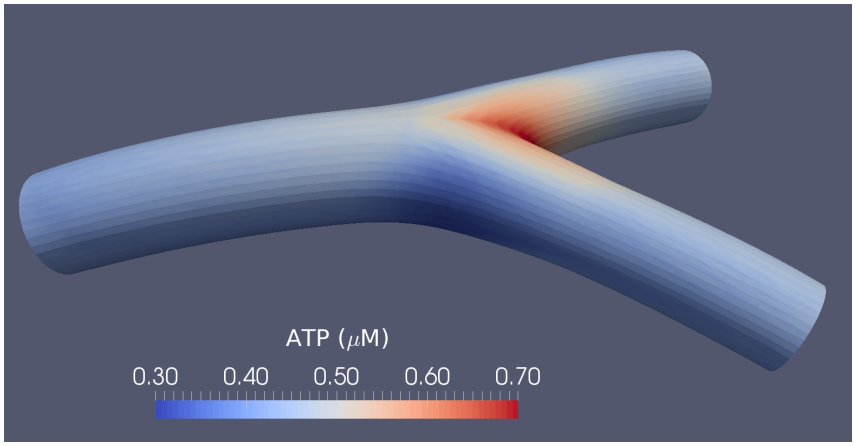

(a) 50° bifurcation angle.

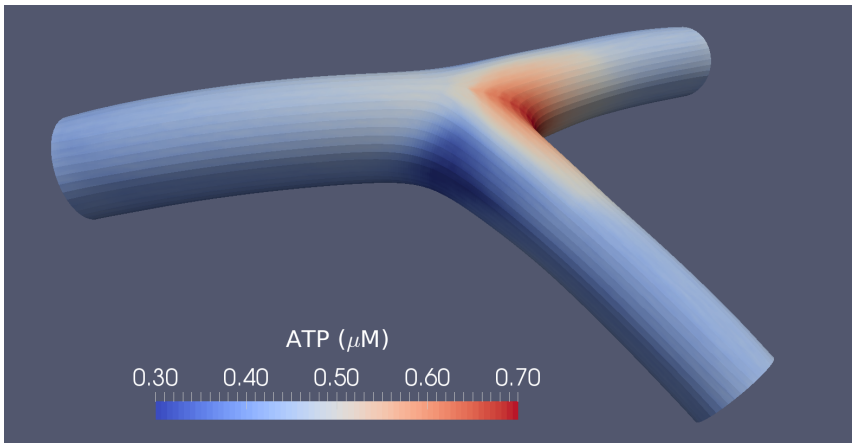

(b) 80° bifurcation angle.

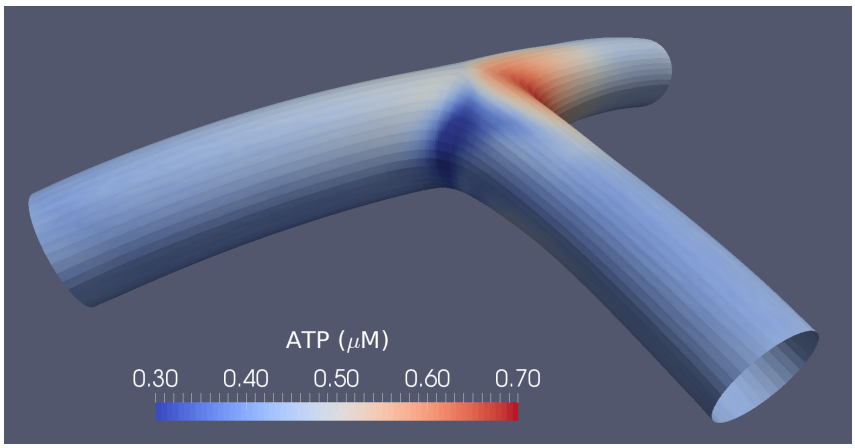

(c) 110° bifurcation angle.

Figure 3.7: Time-averaged ATP maps for three arterial segments with 50°, 80°, and 110° angled bifurcations generated using CFD.

3.3 Coupled Cells Model

The coupled cells model provided by Shaikh et al. (2012) is a platform that enables massively parallel, large scale simulations to be run. At the heart of these simulations is the physiological model of ECs and SMCs provided by Koenigsberger et al. (2005). This section presents an overview of this model, gives the important governing equations, and describes extensions to it.

3.3.1 EC/SMC Unit

The adhesion of agonistic ATP to the endothelial surface within the lumen results in a complex cascade of reactions and movements of chemical species in both ECs and SMCs. The following is a brief description of the modelled participating pathways, where the numbers correspond to those in Figure 3.8.

(1) ATP binds to the purinergic P2Y receptors on the EC surface, activating the G-protein-coupled receptors (GPCR) which then activates a membrane-bound enzyme, phospholipase C (PLC). PLC activation results in the phosphorylation of PIP_2.

(2) PIP_2 gives rise to IP_3 which is then released in the cytosol. This nascent IP_3 binds to IP_3 receptors on the ER/SR surface.

(3) IP_3-bound IP_3-receptor induces release of Ca^{2+} ions from the ER/SR into the cytosol.

(4) Ca^{2+} release from intracellular store sensitises the IP_3-receptor further which releases more Ca^{2+}, thus making a Ca^{2+} rich domain in the cytosol in both EC and SMC. The excess of intracellular Ca^{2+} depolarises the membrane potential. This is know as calcium-induced calcium release (CICR).

(5) ER/SR have low-affinity binding sites on the cytosolic side of a channel which constitutes a pump called the sarco/endoplasmic reticulum Ca^{2+}-ATPase (SERCA) pump. This SERCA pump requires ATP as it is moving Ca^{2+} against the concentration gradient. Cytosolic Ca^{2+} encourages the replenishment of the intracellular stores via this pathway.

(6) Ca^{2+} leaks from ER/SR consistently under a concentration gradient between cytosolic and ER/SR luminal Ca^{2+} and keeps the Ca^{2+} in equilibrium during a non-stimulated state of the cell.

(7) In an EC, the cytosolic Ca^{2+} favours the influx of extracellular Ca^{2+} from non-selective cation channels.

(8) The SERCA pump pushes out cytosolic Ca^{2+} back into the SR.

(9, 10) In ECs, activation of KCa, upon binding to Ca^{2+} ions intracellularly at BKCa and SKCa, allow K^+ ions to move out of the cytosol. This hyperpolarises the membrane potential.

(11) Although K^+ ion cellular efflux is the main repolarising current, residual current (mainly consisting of monovalent ions) also contributes to the membrane potential

repolarisation.

(12) The IP_3 concentration increases in the SMC cytosol via transmission of IP_3 from coupled ECs. This IP_3 increase activates the downstream IP_3-induced Ca^{2+} release.

(13) The IP_3 induced and CICR Ca^{2+} depolarises the membrane potential.

(14) The membrane depolarisation results in the influx of Ca^{2+} from voltage-operated calcium channels (VOCCs) which will close upon repolarisation in the following steps.

(15) Ca^{2+}, in addition to other pathways, is pushed out via Na/Ca exchanger.

(16) Binding of Ca^{2+} ions to K_{Ca} opens BKCa channels in the SMC causing K^+ ionic efflux and membrane repolarisation.

(17) Influx of ionised chloride (Cl^-) ions adds to the repolarisation.

(18) The medium for intercellular communication via homocellular gap junctions can either be Ca^{2+}, IP_3 or membrane potential coupling.

(19) Heterocellular gap junctions can couple an EC to an SMC via Ca^{2+}, IP_3 or membrane potential coupling. Hyperpolarised EC membrane potential can hyperpolarise the SMC plasma membrane and consequently close VOCCs.

3.3.2 Key Equations

The underpinning mathematics responsible for modelling coupled cells physiology is taken from Koenigsberger et al. (2005). It consists of ODEs describing the concentration of chemical species in both ECs and SMCs, as well many fluxes and parameters. The ODEs and descriptions of the relevant fluxes, where they first appear, are provided below. The complete list of algebraic constants and full definitions for all fluxes are found in Appendix A.

In a single SMC, cytosolic calcium concentration (c), SR calcium concentration (s), membrane potential (v), cytosolic IP_3 concentration ($\mathcal{I}$), and the open state probability of the calcium-activated potassium channels (ω) are described by the following:

$$\frac{dc}{dt} = J_{IP_3} - J_{SR\_uptake} + J_{CICR} - J_{eff} + J_{leak} - J_{VOCC} + J_{Na/Ca}, \tag{3.8}$$

where J_{IP_3} is the IP_3-induced Ca^{2+} release, J_{SR_uptake} is the Ca^{2+} transfer back into the SR via the Ca^{2+}-activated SERCA pump, J_{CICR} is the Ca^{2+}-induced Ca^{2+} release from the SR into the cytosol, J_{eff} is the removal of intracellular Ca^{2+} through the plasma membrane Ca^{2+}-ATPase (PMCA) pump, J_{leak} is the Ca^{2+} leak from the SR, J_{VOCC} is the influx of extracellular Ca^{2+} via VOCC, and $J_{Na/Ca}$ is the efflux of Ca^{2+} via the Na^+/Ca^{2+} exchanger.

$$\frac{ds}{dt} = J_{SR\_uptake} - J_{CICR} - J_{leak}, \tag{3.9}$$

$$\frac{dv}{dt} = \gamma \left(-J_{Na/K} - J_{Cl} - 2J_{VOCC} - J_{Na/Ca} - J_K \right), \tag{3.10}$$

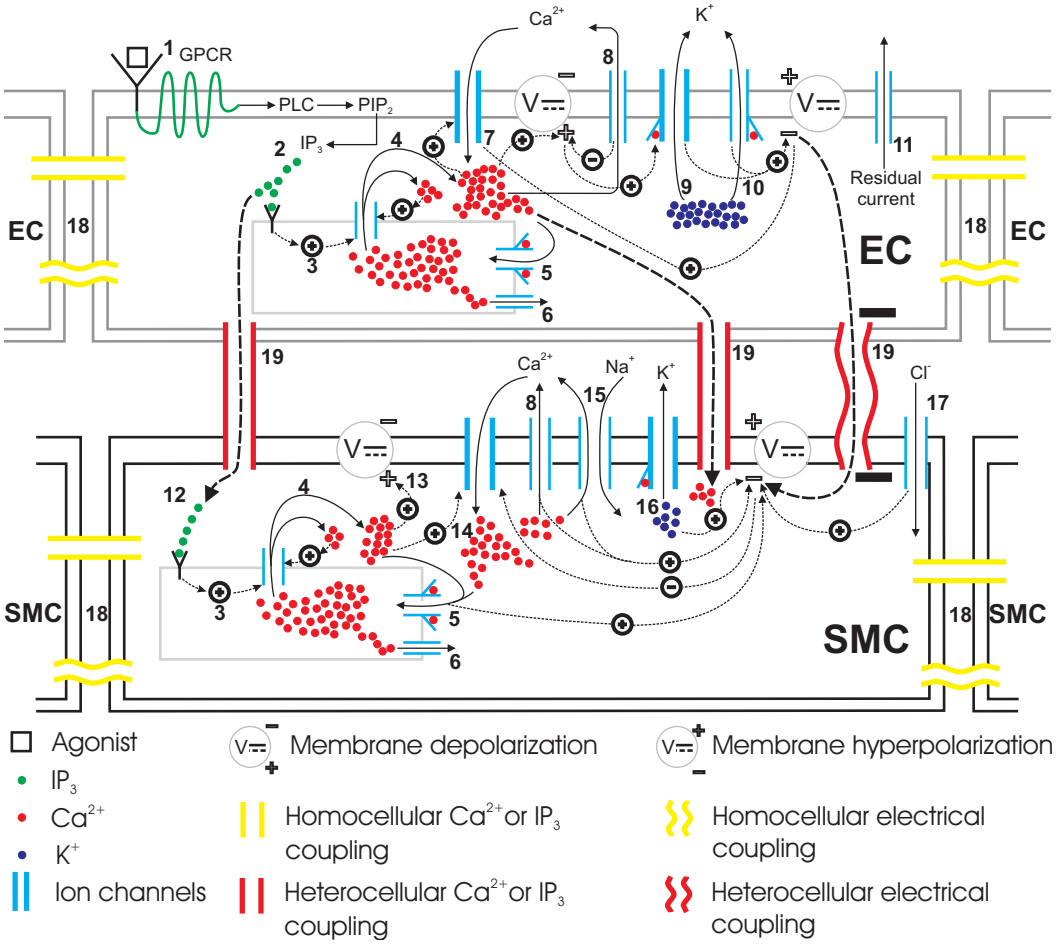

Figure 3.8: Schematic representation of mass transfer dynamics in a single coupled EC/SMC unit. The diagram is adapted from Shaikh et al. (2012). The numbers refer to the pathways described in the text.

where $J_{Na/K}$ is the constant rate efflux of potassium through the Na^+/K^+ pump, J_{Cl} is the influx of chloride ions caused by the plasma membrane depolarisation, and J_K is the potassium efflux through the plasma membrane-bound BK_{Ca} channels.

$$\frac{d\mathcal{I}}{dt} = J_{PLC} - J_{degrade}, \tag{3.11}$$

where J_{PLC} is the input agonist concentration, and $J_{degrade}$ is the linear IP_3 concentration degradation.

$$\frac{d\omega}{dt} = \lambda \left(K_{activation} - \omega \right), \tag{3.12}$$

where $K_{activation}$ is a function of the Ca^{2+}-activated K^+ channels determined by the cytosolic Ca^{2+} concentration, and ω is the open channel probability of the Ca^{2+}-activated channels expressed as a function of $K_{activation}$.

Cytosolic calcium, membrane potential, and IP_3 are coupled between adjacent SMCs

with the following equations:

$$J_{c-coupling_i} = -p_{Ca} \sum_j (c_i - c_j), \tag{3.13}$$

$$V_{coupling_i} = -g \sum_j (v_i - v_j), \tag{3.14}$$

$$J_{I-coupling_i} = -p_{IP_3} \sum_j (I_i - I_j), \tag{3.15}$$

for each SMC i to neighbouring SMCs j. These are appended to their corresponding ODE equations, (3.8), (3.10), (3.11) respectively.

In an EC, cytosolic calcium concentration ($\tilde{c}$), SR calcium concentration ($\tilde{s}$), membrane potential ($\tilde{v}$), and cytosolic IP_3 concentration ($\tilde{\mathcal{I}}$) are modelled by:

$$\frac{d\tilde{c}}{dt} = \tilde{J}_{IP_3} - \tilde{J}_{ER\_uptake} + \tilde{J}_{CICR} - \tilde{J}_{eff} + \tilde{J}_{leak} - \tilde{J}_{cation} + \tilde{J}_0, \tag{3.16}$$

where $\tilde{J}_{IP_3}$ is the IP_3-induced Ca^{2+} release, $\tilde{J}_{ER\_uptake}$ is the Ca^{2+} transfer back into the ER via the Ca^{2+}-activated SERCA pump, $\tilde{J}_{CICR}$ is the Ca^{2+}-induced Ca^{2+} release from ER into cytosol, $\tilde{J}_{eff}$ is the removal of intracellular Ca^{2+} through the PMCA pump, $\tilde{J}_{leak}$ is the Ca^{2+} leak from ER, $\tilde{J}_{cation}$ is the calcium influx through non-selective cation channels, and $\tilde{J}_0$ is a constant Ca^{2+} influx.

$$\frac{d\tilde{s}}{dt} = \tilde{J}_{ER\_uptake} - \tilde{J}_{CICR} - \tilde{J}_{leak}, \tag{3.17}$$

$$\frac{d\tilde{v}}{dt} = -\frac{1}{\tilde{C}_m}\left(\tilde{J}_K + \tilde{J}_{residual}\right), \tag{3.18}$$

where $\tilde{J}_K$ is the constituent currents determined by the potassium efflux through large and small Ca^{2+}-activated channels, and $\tilde{J}_{residual}$ is the residual current comprising an inward sodium or potassium current and an outward chloride current.

$$\frac{d\tilde{\mathcal{I}}}{dt} = \tilde{J}_{PLC} - \tilde{J}_{degrade}, \tag{3.19}$$

where J_{PLC} is the input agonist, and $\tilde{J}_{degrade}$ is the linear IP_3 concentration degradation.

Similar to the SMC model, cytosolic calcium, membrane potential, and IP_3 are heterocellularly coupled between neighbouring ECs. The following equations describe this coupling:

$$\tilde{J}_{c-coupling_i} = -\tilde{p}_{Ca} \sum_j (c_k - c_l), \tag{3.20}$$

$$\tilde{V}_{coupling_i} = -\tilde{g} \sum_j (v_k - v_l), \tag{3.21}$$

$$\tilde{J}_{I-coupling_i} = -\tilde{p_{IP_3}} \sum_j (I_k - I_l), \tag{3.22}$$

for each EC k to neighbouring ECs l. This is appended to its corresponding ODE equation, (3.18).

The same three species, cytosolic calcium, membrane potential, and IP_3, are also heterocellularly coupled. Between an SMC i to its neighbouring ECs l, and an EC k to its neighbouring SMCs j, the equations

$$V^{SMC\to EC} = -G \sum_l (v_i - \tilde{v_l}) \quad and \quad V^{EC\to SMC} = -G \sum_j (\tilde{v_k} - v_j), \tag{3.23}$$

$$J^{SMC\to EC} = -P_{Ca} \sum_l (c_i - \tilde{c_l}) \quad and \quad J^{EC\to SMC} = -P_{Ca} \sum_j (\tilde{c_k} - c_j), \tag{3.24}$$

$$J^{SMC\to EC} = -P_{IP_3} \sum_l (I_i - \tilde{I_l}) \quad and \quad J^{EC\to SMC} = -P_{IP_3} \sum_j (\tilde{I_k} - I_j), \tag{3.25}$$

are added to equations (3.10) and (3.18), (3.8) and (3.16), and (3.11) and (3.19) respectively.

All parameters within the coupling equations are determined by particular coupling cases, whose values can be found in Table A.3, Appendix A. Cases 1 and 2 reflect *healthy* (non-pathological) coupling cases, where Case 2 has the added heterocellular Ca^{2+} coupling. The remaining two coupling configurations are designed to simulate pathological cases. In Case 3, IP_3 coupling is added to the default homocellular EC coupling to simulate upregulation of Cx43 in lesion-prone areas, as described in the work of Burnier et al. (2009). Case 4 has the homocellular EC and heterocellular membrane potential Ca^{2+} coupling disabled to simulate the coupling in progressive atherosclerosis when Cx43 connexin is the dominant mechanism of intercellular communication due to the downregulation of Cx37 and Cx40 connexins (Brisset et al., 2009). It is recognised that these four cases represent simple approximations of complex physiological phenomena and should not be seen as a complete description of the mechanisms involved. Figure 3.9 displays Hopf bifurcations for the system using each of these coupling cases.

3.3.3 Extensions to the Model

There exist many mathematical models in this field of research, and often those modelling the same physiology can differ in their assumptions, simplifications, and details deemed important. While reviewing a selection of related works, potential improvements to our model were found. These included a more detailed description of the ATP pathway, such as those found in Lemon et al. (2003) and Bennett et al. (2005), and the definition of gap-junction currents from Jacobsen et al. (2007). To ensure the simulations presented below were as accurate as possible, these two elements have been implemented into the model used here.

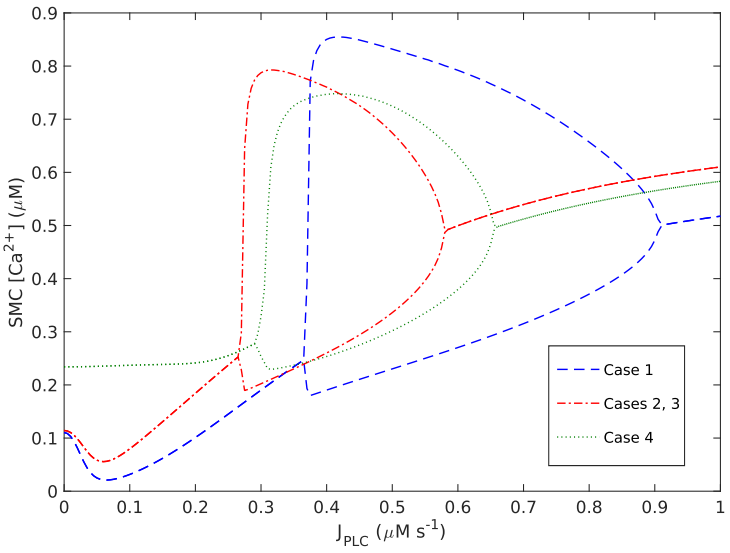

Figure 3.9: Bifurcation diagram for cytosolic SMC Ca^{2+} concentration in a single coupled EC/SMC unit as function of increasing ATP at the EC surface for coupling cases 1–4.

ATP Pathway

The generation of IP_3 from agonistic molecules binding to endothelial receptors contains a number of complex intermediate reactions, most of which are ignored in the EC/SMC model of Koenigsberger et al. (2005) who assumed a linear relationship between ATP and IP_3. In contrast, both Lemon et al. (2003) and Bennett et al. (2005) described the ATP pathway in greater detail, though with some variation in complexity, and both with potential shortcomings.

The model presented by Bennett et al. (2005) relies heavily on the production rate of IP_3; a constant determined experimentally. This value is dominant in determining the cellular IP_3 concentration, and as such may lead to anomalies when used in future simulations. Furthermore, the secondary effect of Ca^{2+} on IP_3 production by activation of PLC is ignored.

Conversely, the model provided by Lemon et al. (2003) is highly complex and relies less on experimentally fitted constants. However, the complexity is perhaps too great. The authors note many of the parameters in the receptor binding model have unknown values and are treated as free variables. A balance between the two has been reached with the creation of a hybrid model—joining their best features while omitting possible drawbacks. An overview of this hybrid model, including its equations and the processes they describe, follows.

The pathway begins with ATP binding to P2Y receptors. The model presented in Bennett et al. (2005) assumed these receptors do not desensitise—that they are neither phosphorylated nor recycled. Consequently, the ligand/receptor binding can be simplified to

$$L + R \underset{k_1^-}{\overset{k_1^+}{\rightleftarrows}} LR, \tag{3.26}$$

where L is the ligand (ATP) and R is the receptor (P2Y). The ratio of bound to total receptors, with fast kinetics binding assumed, is

$$\rho_{P2Y} = \frac{[ATP]}{K_{ATP} + [ATP]}. \tag{3.27}$$

Here, K_{ATP} is the effective Michaelis-Menten constant for ATP binding to a P2Y receptor and $[ATP]$ is the lumenal ATP concentration.

Lemon et al. (2003) describe the G-protein cascade in detail. This involves the activation of G-protein and PLC, the subsequent hydrolysis of PIP_2 to IP_3 and DAG, and the replenishment of PIP_2 in the cytosol.

The dynamics of activated G-protein are described with:

$$\frac{dG_{prot}}{dt} = k_a \cdot (\delta + \rho_{P2Y}) \cdot (G_{prot_{tot}} - G_{prot}) - k_d \cdot G_{prot}, \tag{3.28}$$

where k_d and k_a are the deactivation and activation rates of G-protein respectively, $G_{prot_{tot}}$ is the total number of G-protein molecules within the EC, and δ is the G-protein intrinsic activity parameter.

Lemon et al. (2003) considered that PLC induces the hydrolysis of PIP_2, and that it is only able to do so when fully activated. Therefore, with the assumption of fast kinetics, the hydrolysis rate of PIP_2 can be calculated as

$$r_h = \alpha \left(\frac{[Ca^{2+}]}{[Ca^{2+}] + K_{Ca}} \right) G_{prot}, \tag{3.29}$$

where K_{Ca} is the dissociation constant for Ca^{2+} binding to PLC, $[Ca^{2+}]$ is the cytosolic concentration of Ca^{2+} in the EC, and α is an effective signal gain parameter which was fitted to experimental data (and is treated as a constant).

While Lemon et al. (2003) calculated the number of PIP_2 molecules in the cell membrane, its concentration during agonist-stimulation has been observed to be relatively constant in preliminary simulations. As such, the constant value $PIP_{2_{tot}} = 5.0 \times 10^7$ is used (Johny, 2016; Johny et al., 2017).

Finally, the IP_3 dynamics taken from Lemon et al. (2003) are described by:

$$\frac{dI}{dt} = \frac{r_h PIP_{2tot} \cdot unitcon_B}{N_a \cdot V_{EC}} - J_{degrade} \tag{3.30}$$

where Avogadro's constant N_a, volume of the cell v, and $unitcon_B$ are used to convert the number of IP_3 molecules to a molar concentration. All parameter values for the implemented IP_3 pathway are found in Table A.4, Appendix A.

Gap-Junction Currents

Another simplification in the physiological model of Koenigsberger et al. (2005) is the diffusion of membrane potential between cells. Membrane potential is a phenomenon that exists due to the imbalance of charge between two separated bodies resulting in an electrical gradient between them. This property cannot be diffused. Instead, ionic species carrying charge are diffused, which in turn alters the membrane potential. As opposed to diffusing membrane potential, Jacobsen et al. (2007) described the existence of gap-junction currents due to both membrane potential and concentration gradients between neighbouring cells. This is done with the following equation:

$$I_{gap,x} = P_x \sigma A_{segment} F \Big[\Delta[x] + \Big(\frac{zF\overline{[x]}}{RT} \Delta V_m \Big) \Big]. \tag{3.31}$$

Here, $\overline{[x]} = ([x]_a + [x]_b)\ /\ 2$ is the average concentration of ion x between two cells, a and b, $\Delta V_m = V_{m,a} - V_{m,b}$ is the membrane potential gradient, and $\Delta[x] = [x]_a - [x]_b$ is the concentration gradient of ion x. The concentration gradient here is only relevant for Ca^{2+}, as intracellular concentrations of all other ions are assumed to remain constant on the considered time scale. z is the valence of ion x, F is Faraday Constant, T is the absolute temperature, P_x is the permeability of ion x, and R is the universal gas constant. These gap-junction currents coexist with the Fickian diffusion of IP_3 and Ca^{2+} in our model—only diffusion of membrane potential has been removed.

In the model used by Jacobsen et al. (2007), each cell is divided into 120 segments along its length axis. $A_{segment}$ is the surface area of a given segment, and where two segments that make contact between cells are of different surface area, the smaller area is used. σ is approximately the fraction of the cell boundaries in contact. These parameters are closely tied to the geometry of the cells in their model—being elongated hexagonal in shape and connected to six other cells homocellularly. There are a few noteworthy differences in our model, compared to that of Jacobsen et al. (2007). The gap-junction current equations therefore required modification before integration. The first consideration is the different cellular structures; both ECs and SMCs are rectangular and communicate with four adjacent cells in our model. The other is heterocellular communication resulting from the existence of two different cell types. An individual EC or SMC communicates with many more cells heterocelluarly than homocellularly due to these cells' relative orthogonal alignments, and this feature must be recognised in the gap-junction equation.

$A_{segment}$ has been replaced with $A_{average} = (A_{cell_a} + A_{cell_b})/2$, the averaged area of two communicating cells. This varies for different cell types in contact, where an EC and SMC have areas 200 and 500 μm^2 respectively (Kapela et al., 2008; Silva et al., 2007). σ has been modified to vary for homocellular and heterocellular communication. The values for the parameters in the final implementation of the gap junction currents equation can be found in the Appendix, Table A.5.

3.4 Parallel Implementation

The physiological model presented in the previous section is responsible for the behaviour of coupled cells on a micro-scale, notably in the dynamics within individual cells, and in communication between adjacent cells. The techniques and strategies that allow this model to be run in parallel and on a macro-scale are presented in this section.

A parallel coupled cells simulation requires as input the geometric configuration of a bifurcation surface, in terms of the number of quadrilaterals along axial and circumferential dimension. In addition, each simulation requires the configuration of the coupled EC and SMC within a quad. The quadrilaterals are grouped into 2-D Cartesian surface-meshes, each representing a tubular segment/branch of a bifurcation. Within each 2-D Cartesian mesh, the quadrilaterals correspond to computational domains that are mapped to distinct MPI tasks. A periodic boundary condition is imposed along the longitudinal edge of each 2-D Cartesian grid. In this case, the periodic boundary condition refers to the MPI-enabled communication-specific mapping of MPI tasks.

The system of ODEs within each quadrilateral domain is solved at every specified time-step, the value of which is set in the configuration file. The solving is performed by Sundials' ARKode (Hindmarsh et al., 2005), and is done so numerically, as opposed to analytically. ARKode uses additive Runge-Kutta methods, which enables it to split an ordinary differential equation into its slow and fast time-scale components. Consequently, these components can be solved using explicit and implicit methods, respectively. In particular, ARKode solves ordinary differential equations with the form

$$\dot{y} = f_E(t, y) + f_I(t, y), \qquad y(t_0) = y_0,$$

where y is a vector of solution components and t is the independent variable. Either component on the right hand side can be zero, which allows for fully explicit, fully implicit, or combination explicit-implicit time integration. With regard to our physiological model, the membrane potential in both ECs and SMCs are solved implicitly, and all other species explicitly. This decision followed the plotting of all ODEs, and observation of the relative differences in time-scales.

At regular time intervals the state variables from the cells along the edges of the quadrilateral domains are passed to the adjacent cells in the neighbouring domains. The inter-domain communication was implemented through the MPI library, the solution of which follows the mesh ghost cell communication pattern recommended for discretised domain decomposition (Gropp et al., 2014). Each quadrilateral domain contains additional vectors of ghost cells to store the values from neighbouring domains (Figure 3.10). For the simulations presented in this thesis, the inter-domain communication interval was set to 0.01 seconds. This interval was chosen to maintain the balance between MPI communication and computation times.

Values of state variables for ECs and SMCs are written to HDF5 format after every elapsed physiological second. A single core per branch is assigned the role of gathering all state values and subsequently writing them out as HDF5 files. During post-processing, the

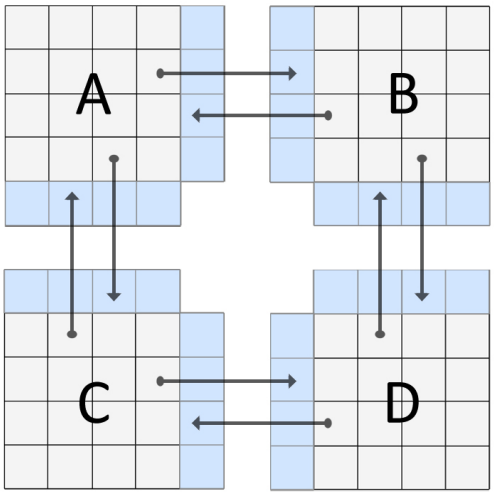

Figure 3.10: An overview of the ghost cell communication pattern with four computational domains A, B, C, and D. Ghost cells coloured blue obtain neighbouring domain values at periodic time intervals.

HDF5 output data are mapped onto the surface/cell mesh and written out in VTK's VTU format, an XML-based format with binary data for unstructured grid data. Visualisations and analysis were performed with ParaView (Ayachit, 2015).

3.4.1 Modifications to the Parallel Implementation

The current parallelisation strategy, in particular the domain decomposition, is limiting the scale of our simulations. Previous use of the (now decommissioned) Blue Gene/P allowed for single bifurcation simulations involving approximately 600,000 ECs, and 1,600,000 SMCs. In comparison, one direction of this research aims to simulate multiple bifurcations, up to the entire coronary tree. This scale of simulation would contain the order of one hundred million endothelial and smooth muscle cells. With our current parallel implementation, this would require a supercomputer with over half a million cores.

To achieve simulations orders of magnitude larger, modifications are necessary. Such modifications include: efficiency improvements to existing strategies, the introduction of new technologies, and creating flexible simulation code resulting in less overhead when porting to new architectures.

Another important consideration is obtaining access to more powerful supercomputers. To be eligible for particularly large platforms, simulation code must display both strong and weak scaling, as well as general efficiency where possible. Not only are sizeable modifications for future simulation necessary, but so are smaller modifications that decrease current simulation times. Descriptions of the various improvements made to the parallel implementation follow, while the results of these modifications can be found in Chapter 4.

Variable Domain Decomposition

Simulations were previously strongly tied to the exact geometry of an arterial mesh; in particular, to the number of quadrilaterals comprising the geometry, as well as to the number of cells in each quad. As a result, the number of processor cores was fixed for each mesh, given the one-to-one mapping of quadrilaterals to processor cores.

This dependency between domain-decomposition and mesh-generation is both unnecessary and limits the scale of simulations. Variable domain decomposition was introduced to uncouple these elements, which allows a parameterised number of quadrilaterals in the axial and circumferential directions to be joined at run time. With this approach, the number of cells each processor core is responsible for, and consequently the number of required cores for the entire mesh, is dynamic.

This extension carries with it a number of benefits, for both present and future simulations. Larger simulations can be run on machines with fewer cores by over-subscribing the work for each core. The ability to run larger simulations comes at the cost of longer simulation times, such that the number of quadrilaterals joined scales exactly with the increase in simulation time (see Figure 3.11). For example, the Blue Gene/P machine contained 8192 processor cores, while the P575/POWER6 (Fitzroy) contains fewer. In particular, 108 nodes each with 32 cores (3,456 4.7 GHz processor cores), with each node having either 64 or 128 GB RAM. However, identically sized simulations can be run on Fitzroy using fewer numbers of quadrilaterals containing a greater number of cells.

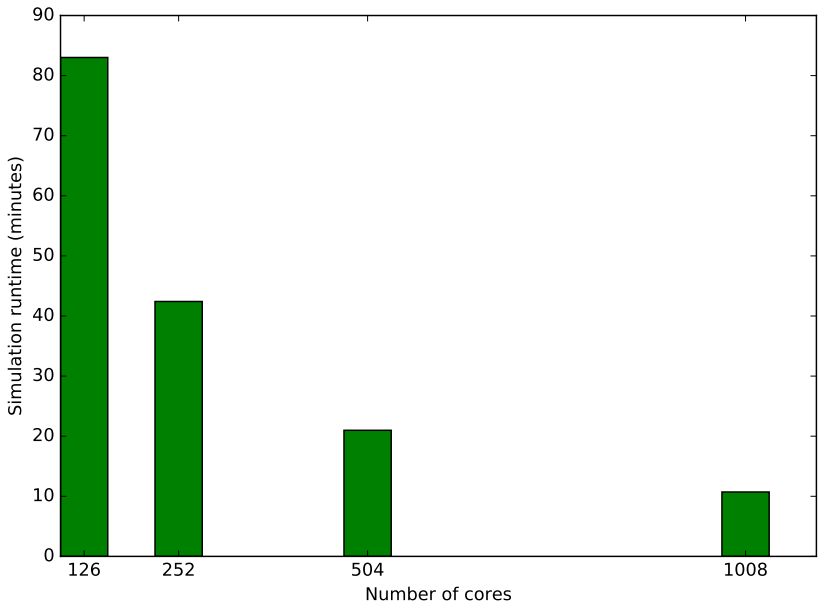

Figure 3.11: Strong scaling results for a 1008-quadrilateral simulation using varying sized quadrilaterals. Simulations were performed on the P575/POWER6 machine, Fitzroy.

This strategy is a stepping-stone towards further scalability and performance improvements. Improvements to workload distribution within individual cores can become more valuable by over-subscribing the work for each processor (for example, with the introduc-

tion of threading). The combination of assigning cores an increased workload, and further distributing this work across multiple threads, will allow for simulations of superior scale. One such multi-threading technology is Open-Multi-Processing (OpenMP), and is the next subject of modification.

OpenMP

Until now, the Coupled Cells parallel implementation has only used multiple processes. Further parallelisation is possible, with the use of threading. A thread of execution is a sequence of instructions within a single process; multiple threads can exist per process. They can run (seemingly) in parallel by means of fast context switching, controlled by the processor's scheduler, and use a shared address space.

To utilise multiple threads, application programming interfaces (APIs) such as OpenMP were created. These provide simple and flexible interfaces for programmers to parallelise code within single processes. In the context of this research, OpenMP could be introduced to reduce simulation time. However, it is important to note multi-threading does not always improve performance. Employing multiple threads comes with computational overhead—their creation, ensuring race-conditions do not occur, and context switching between them. If an improvement is to be found with its introduction to our code, a greater understanding of our simulations, including the relative costs of each procedure, is necessary. This requires instrumentation using specialised profiling tools, and was achieved with Tuning and Analysis Utilities (TAU) (Shende and Malony, 2006), a toolkit for analysis of parallel programs, capable of gathering detailed performance information. Figure 3.12 displays a benchmark analysis of a relatively small simulation, with which we discovered the relative computational costs of each procedure.

The two most expensive procedures reported by TAU were `koenigsberger_ec_explicit` and `koenigsberger_smc_explicit`. They consist of nested for-loops, and are responsible for calculating the relatively slow time-scale fluxes for all ECs and SMCs within a quadrilateral, respectively. These procedures show the greatest potential for improvement with the introduction of multiple threads, and were therefore targeted.

OpenMP provides numerous methods of parallelising code; one such method collapses nested loops, and splits the tasks within the inner loop between a number of threads. Collapsing a nested loop transforms the following

```
for (int i = 0; i < N; i++) {
   for (int j = 0; j < M; j++) {
   ...
```

into

```
for (int k = 0; k < N * M; k++) {
   int i = k / M; // Iterates through [0,N-1] using floor division.
   int j = k % M; // Loops through [0,M-1] using modular arithmetic.
   ...
```

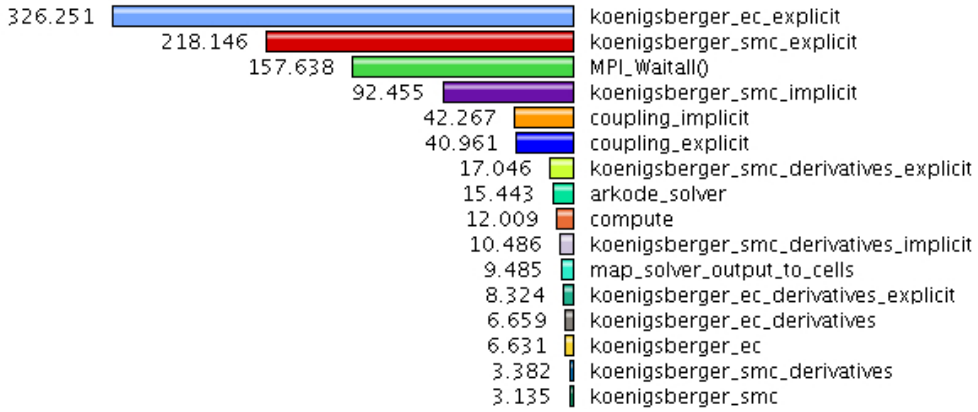

Figure 3.12: TAU's visualisation tool *paraprof* showcasing the computational costs of multiple procedures during a 100 physiological-second-simulation. The values on the left are in seconds, and the names on the right are those of the procedures. The simulation was performed on the P575/POWER6 machine, Fitzroy.

for some values N and M. If the condition of independent inner loop tasks is met, the chosen number of threads can perform these tasks in parallel—each with unique sets of i and j values within the domain. With respect to our simulation's two most expensive procedures, the two values of k are the numbers of ECs and SMCs each core is responsible for respectively.

This OpenMP directive, `collapse`, was integrated into our simulations with the goal of reducing the computation time of these procedures. One final consideration was to determine the optimal number of parallel threads. To do this, a series of simulations of variable sizes were run; the results of these can be found in Chapter 4.

MPI Communication Optimisation

To collect all state variables within a writing group onto a single process, the MPI procedure `MPI_Gather`[2] was used. Specifically, the procedure was invoked for each state variable individually. Inter-process communication is relatively expensive, especially synchronous communication where handshaking must occur with all sending processes. To reduce this overhead, the gathering of data was modified so that all communicating processes first collected their state variables in a single contiguous array before sending it to the writer node. The writer node is then responsible for splitting all received arrays into individual state variable arrays, using appropriate offsets. With this technique, the same amount of data is transferred across processes, but it is done with a single call to `MPI_Gather`, rather than multiple calls.

This modification becomes more and more valuable in larger simulations, similar to the introduction of threading. As more quadrilaterals are joined, and more cells exist within each writing group, the overhead of inter-process communication similarly increases. However, with fewer gathers, this increase in overhead will not scale as sharply.

[2] `http://mpi-forum.org/docs/mpi-1.1/mpi-11-html/node69.html`

3.5 Summary

This chapter presented a number of extensions and additions to the components of massively parallel physiological simulations. Details of the unmodified components were also provided, so that all processes in conducting these macro-scale simulations were described.

A mesh generation pipeline capable of creating arterial geometries was developed, using VTK functionality. This pipeline accepts a centreline, synthetic or from patient data, as input and produces vessel surface-meshes of varying geometries and magnitudes. A Python script was created to generate synthetic centrelines of varying complexity, such as the number of branches, their length, the angles between them, and the overall planarity. Three arterial surfaces with differently angled bifurcations were then generated, and used to create input ATP maps from CFD simulations.

Modifications to the physiological model were then introduced, including a detailed IP_3 pathway in ECs, and gap-junction currents between all cells. The IP_3 pathway was predominantly taken from Lemon et al. (2003), although some simplifications found in Bennett et al. (2005) and Johny et al. (2017) were integrated. The equation describing gap-junction currents details the movements of ionic species between cells, and the resulting changes to cellular membrane potential (Jacobsen et al., 2007). This replaced the simplified Fickian diffusion of membrane potential in the earlier model.

Finally, the parallel implementation of our macro-scale simulations was extended with a number of additions. In particular, multi-threading with OpenMP, a method to set the problem size per processor core at runtime, and a technique to potentially reduce communication overhead. To maximise the performance increase provided by OpenMP, the computational costs of all procedures were examined using TAU.

Chapter 4

Results

The results in this chapter are presented in three sections: massively parallel simulations, single-cell dynamics, and computational performance. The first section reports on the macro-scale physiological simulations, which describe emergent properties of coupled arterial cells across bifurcations with varying angles. There is a particular emphasis on Ca^{2+} dynamics in the presentation of these simulations. The second section consists of additions to the underlying mathematical model; these were included to make our current simulations as physiologically accurate as possible. The third section describes modifications to the computational component of our simulations, which aim to improve current performance and provide highly scalable code for future simulations.

4.1 Massively Parallel Simulations

This section presents emergent behaviour of cellular dynamics using massively parallel simulations of arterial bifurcations, following the application of all extensions to individual components described so far. The newly developed mesh generation pipeline was used to generate multiple surface-meshes with varying bifurcation angles, the single-cell model was improved to ensure greater physiological fidelity, and the parallel implementation was extended to accommodate appropriately large-scale simulations. The results from simulations using synthetically generated agonist maps will be presented first, followed by those using the more complex physiologically accurate agonist input.

4.1.1 Synthetic Agonist Maps

Macro-scale simulations were conducted using synthetically generated ATP maps as outlined in Section 3.2.1. These agonist maps were created to simplify the experimental conditions and observe fundamental phenomena, prior to the use of CFD-based input maps. Simulations were performed on the IBM BlueGene P architecture at the University of Canterbury High Performance Computing Centre[1]. Figure 4.1 shows the results of these simulations; in

[1] `http://www.hpc.canterbury.ac.nz/tech_specs/bluegenep.shtml`

particular, Ca^{2+} dynamics in ECs and SMCs at time $t = 300s$. The animated visualisations for these simulations is found here: `https://goo.gl/BGGhJp`.

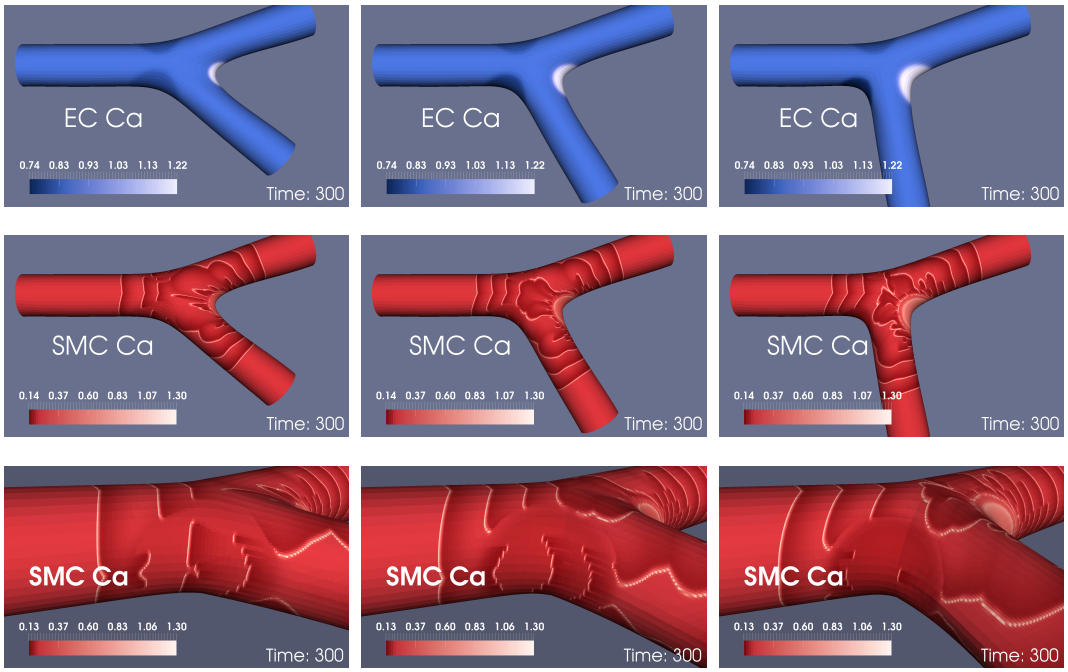

Figure 4.1: 1000-physiological-second simulations of Ca^{2+} dynamics in SMCs (red) and ECs (blue) using 60°, 80°, and 100° geometries and a synthetic ATP input map. Front and side views are provided, at time $t = 300s$.

The EC layer dynamics follow the ATP pattern, while the SMC layer displays oscillatory behaviour. Increasing the bifurcation angle to 100° results in waves ceasing to propagate into the lateral bifurcation seam region, whilst for angles of 60° and 80° waves propagate into this region. For the 60° bifurcation the area displayed wave propagation with either no growth in wave length or slow growth if the initial wave size was large enough. Waves propagating from the bifurcation apex initially move upstream and then propagate circumferentially to form axisymmetric waves in both branches. Waves meeting head-on are destroyed, while spiral waves form when their length is truncated by meeting a low ATP surface concentration.

4.1.2 Physiologically Accurate Agonist Input

The simulations using physiologically accurate input maps were performed on Fitzroy (the architecture of which is described in Section 3.4); the surface-meshes contained 4080 quadrilaterals—over one million cells in total—for which 512 processor cores were used. Approximately five hours was required to complete each 500-physiological-second simulation. In comparison, these simulations would have needed closer to ten hours each using the Blue Gene/P.

Snapshots of Ca^{2+} concentrations in SMCs and ECs for the three bifurcation angles are presented in Figures 4.2, 4.3, and 4.4. For each mesh, front-on and side-on views are provided to highlight dynamics in different sections of the vessel segment. Two time-steps

are provided at $t = 100s$ and $t = 500s$ to demonstrate simulation progression. However, a greater appreciation is gained by viewing the animated visualisations of these simulations, which show cellular dynamics over the whole of each simulation. The YouTube play-list can be found at: `https://goo.gl/h73QKC`.

The waves of propagating SMC Ca^{2+} oscillations were observable in all simulations. They originated from the apex of the bifurcation and travelled down the main stem and branches. The period of these oscillations was approximately 20s, in agreement with values from the single-cell dynamics presented in Section 4.2. The Ca^{2+} waves produced at the apex were rapid and distinct, while those at the lateral bifurcation seams propagated more slowly, sporadically, and over significantly shorter distances. Further, the Ca^{2+} waves within these regions were thinner than those elsewhere on the arterial surface with respect to the number of axial SMCs. The difference in bifurcation angulation appeared to accentuate these observations, most notably the Ca^{2+} dynamics at the lateral seams of the 110° bifurcation geometry. Head-on collisions of Ca^{2+} waves result in the destruction of both waves. Finally, the area affected by this complex Ca^{2+} behaviour appeared to reduce in size as a function of wider bifurcation angles. In contrast to all oscillations in SMCs, the EC Ca^{2+} dynamics quickly reached steady states and did not oscillate.

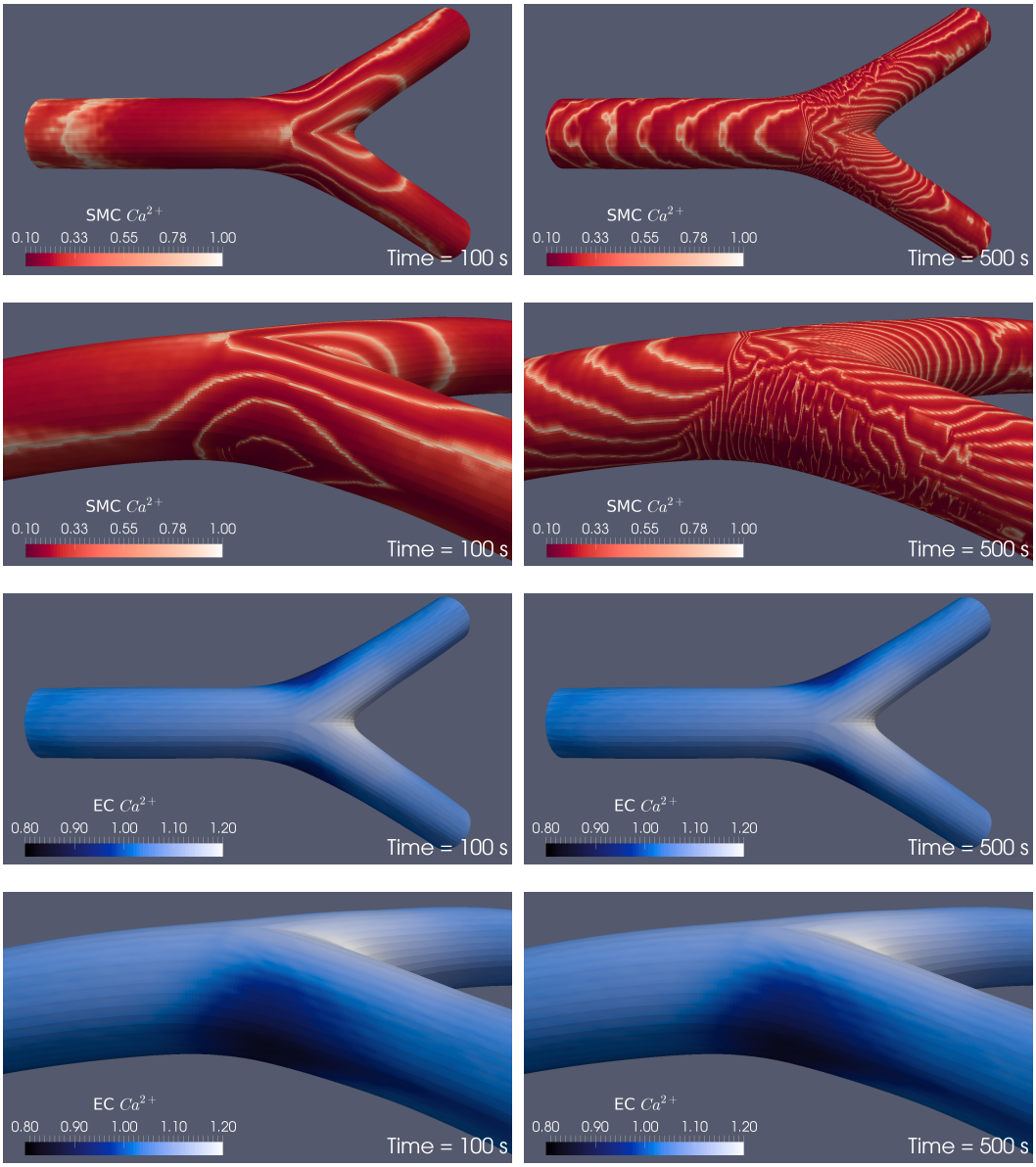

Figure 4.2: 500-physiological-second simulation of Ca^{2+} dynamics in SMCs (red) and ECs (blue) using 50° geometries and a physiological ATP input map. Front and side views are provided, at times $t = 100s$ (left) and $t = 500s$ (right).

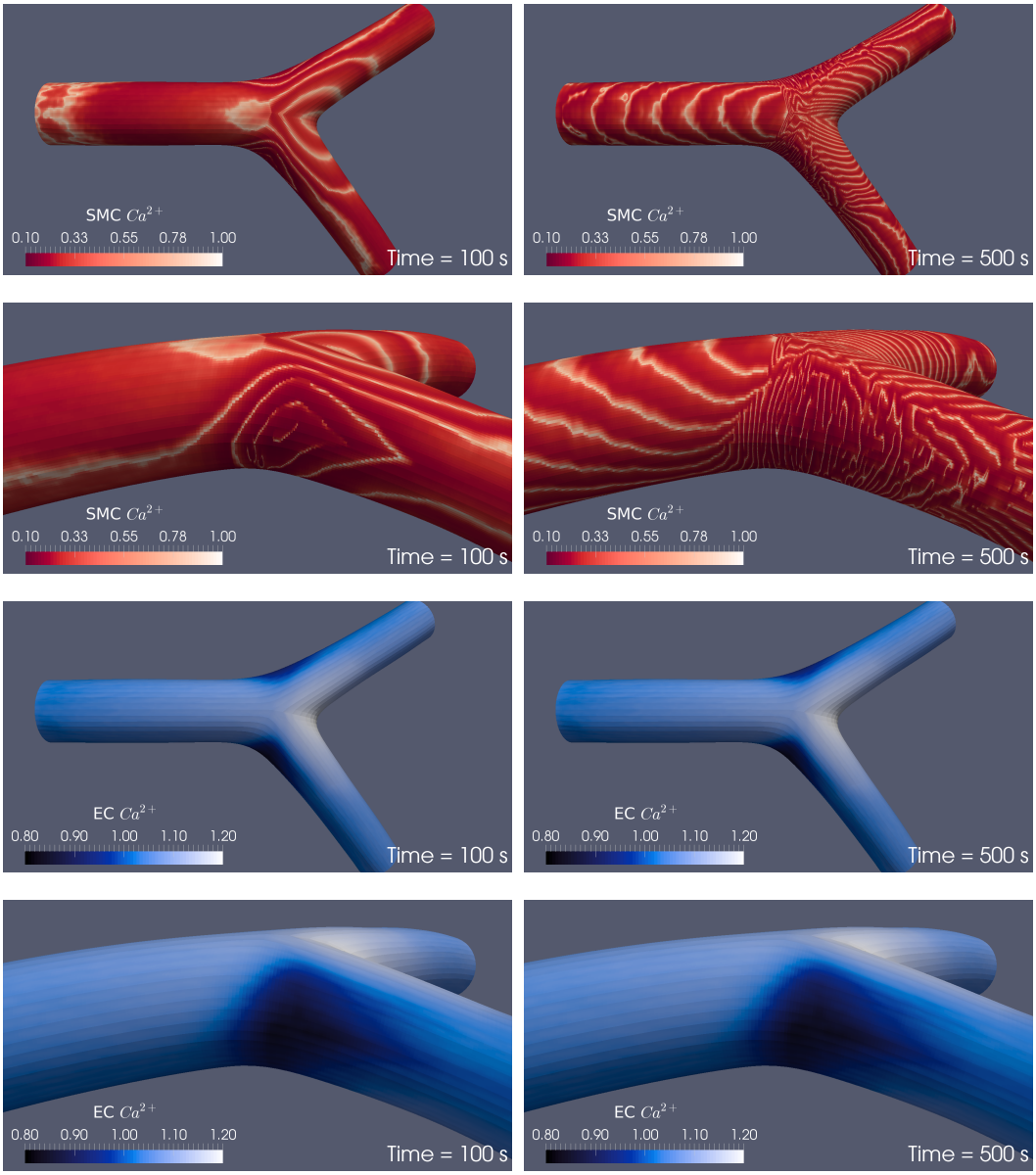

Figure 4.3: 500-physiological-second simulation of Ca^{2+} dynamics in SMCs (red) and ECs (blue) using 80° geometries and a physiological ATP input map. Front and side views are provided, at times $t = 100s$ (left) and $t = 500s$ (right).

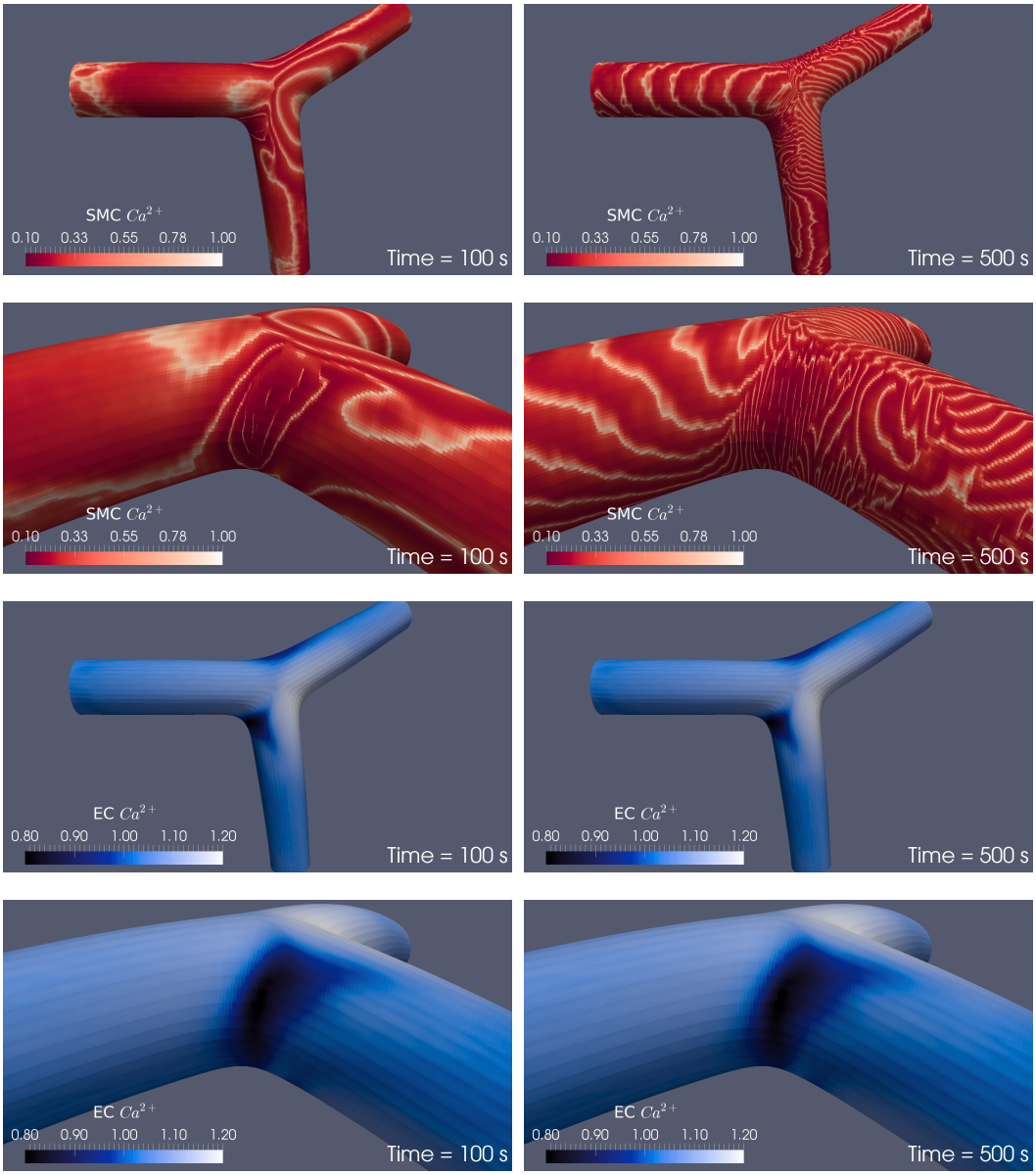

Figure 4.4: 500-physiological-second simulation of Ca^{2+} dynamics in SMCs (red) and ECs (blue) using 110° geometries and a physiological ATP input map. Front and side views are provided, at times $t = 100s$ (left) and $t = 500s$ (right).

Temporal Averaging and Mesh Flattening

The behaviour of SMC Ca^{2+} concentration is fascinating, but difficult to describe quantitatively, especially when examined using a three-dimensional mesh. Further post-processing was therefore performed. First, temporal averaging was applied such that for each cell x in the arterial mesh,

$$\phi_x = \frac{1}{(t_f - t_i)} \sum_{t=t_i}^{t_f} x_{Ca^{2+}}(t). \tag{4.1}$$

Here ϕ_x is the averaged Ca^{2+} concentration in cell x between times t_i and t_f, and $x_{Ca^{2+}}(t)$ is the Ca^{2+} concentration in cell x at time t. Consequently, the frequency and maximum/minimum values of oscillations were averaged to provide a more interpretable account of cellular dynamics. Second, the three-dimensional geometries were mapped to two-dimensional ones, to allow a single perspective to capture SMCs dynamics over the entire arterial segment. The circumferential edges on these surfaces are periodic; this re-mapping can be thought of as an unwrapping of the original geometries. Figure 4.5 demonstrates this transformation for an arbitrary 3-D surface-mesh.

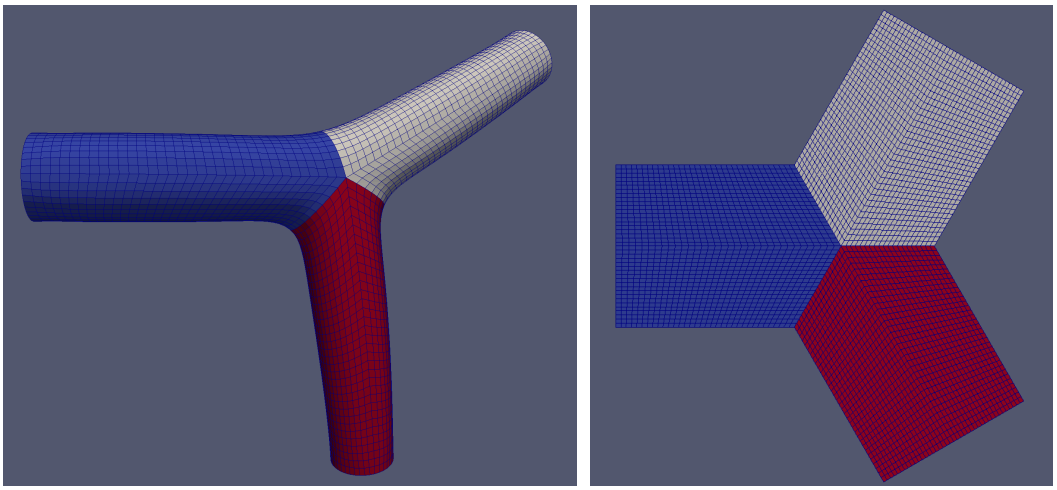

(a) 4080 quadrilateral 3-D mesh. (b) 4080 quadrilateral 2-D mesh.

Figure 4.5: The transformation a 3-D geometry into one that is 2-D. Before (left) and after (right) views are shown with corresponding coloured branches.

The result of applying these post-processing techniques to all three geometries can be seen in Figure 4.6. Temporal averaging is employed over the final 200s of the simulation such that $t_i = 300$ and $t_f = 500$. These values were chosen to maintain a balance between averaging non-transient behaviour, over a sufficiently long period. The results shown in Figure 4.6 confirmed the observation that greater disturbances in Ca^{2+} wave propagation occurred at the lateral seams of bifurcations with greater angles. Further, this temporal averaging disclosed that geometries with smaller bifurcation angles were subject to slightly greater Ca^{2+} concentrations (in peak concentration or oscillation frequency) at the bifurcation apex. This can be seen by comparing the depth of red at the bifurcation apexes in Figures 4.6a and 4.6c.

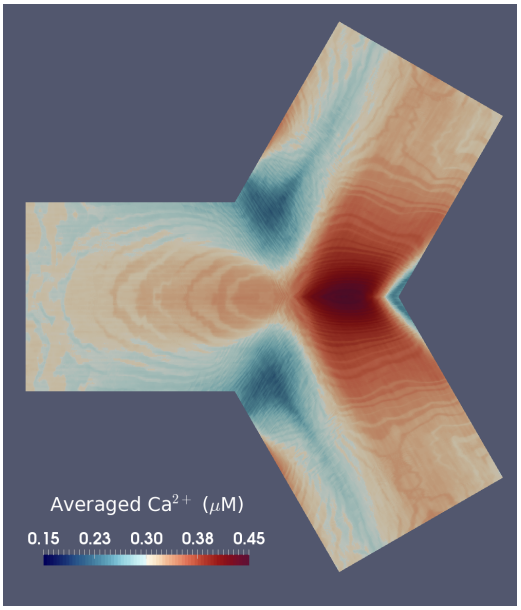

(a) Time-averaged Ca^{2+} dynamics from a 50° bifurcation mesh.

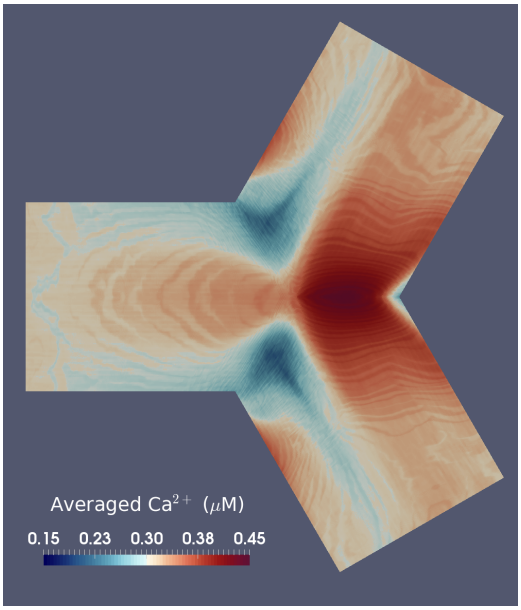

(b) Time-averaged Ca^{2+} dynamics from an 80° bifurcation mesh.

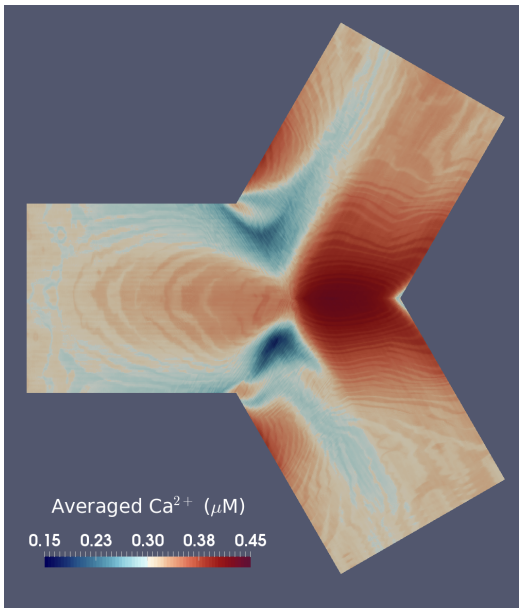

(c) Time-averaged Ca^{2+} dynamics from a 110° bifurcation mesh.

Figure 4.6: Time-averaged SMC Ca^{2+} concentration over 200 physiological seconds using flat mesh re-mappings of geometries with varying bifurcation angles.

4.2 Single-Cell Dynamics

Extensions to the mathematical model were examined by recording all chemical species in a single EC/SMC unit over the course of 150-physiological-second simulations. These simulations included an initial period without stimulation, followed by the introduction of ATP to endothelial receptors. We observed steady states for all species before the introduction of agonistic ATP, after which many displayed oscillatory behaviour, particularly SMC cytosolic Ca^{2+}, and EC/SMC membrane potential.

Figures 4.7 and 4.8 provide comparisons between the original cellular model and that with the newly implemented IP_3 pathway, by examining Ca^{2+} and IP_3 dynamics, while Figure 4.9 presents the newly-added fluxes belonging to this pathway. The general behaviour was unchanged; state variables existed in steady states during the initial period, then many of them transitioned into oscillatory domains following agonistic stimulation. The period of these oscillations has been reduced from 23.6 to 21.6 seconds, approximately a 10% reduction. This is evident when comparing the number of peaks/troughs in the oscillating species to those in the original model. Minor differences in steady-state and peak values are also observable.

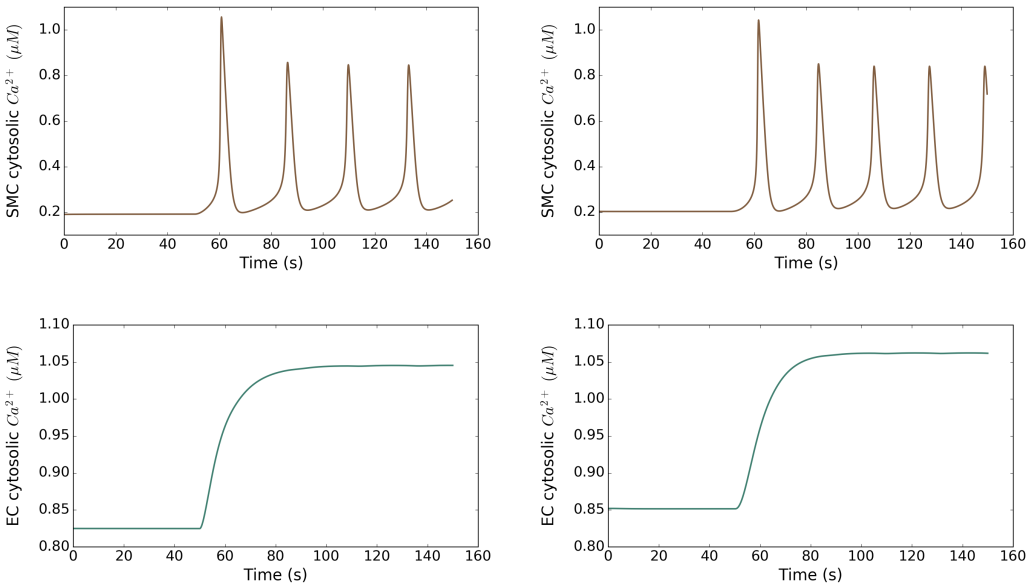

Figure 4.7: Ca^{2+} dynamics in SMCs (top) and ECs (bottom), compared between the original cellular model (left) and that including a detailed IP_3 pathway (right). ATP is introduced at $t = 50s$.

Figure 4.10 shows a comparison between heterocellular Fickian diffusion of membrane potential and heterocellular gap-junction currents. As with the IP_3 pathway additions, results between the two were similar. There appear to be two relatively minor differences: small disturbances at the peaks of oscillations in a range of 0.1–0.2 mV, and there was a shift of approximately +0.5 mV in SMC membrane potential.

The SMC open state probability of the calcium-activated potassium channels, and SR

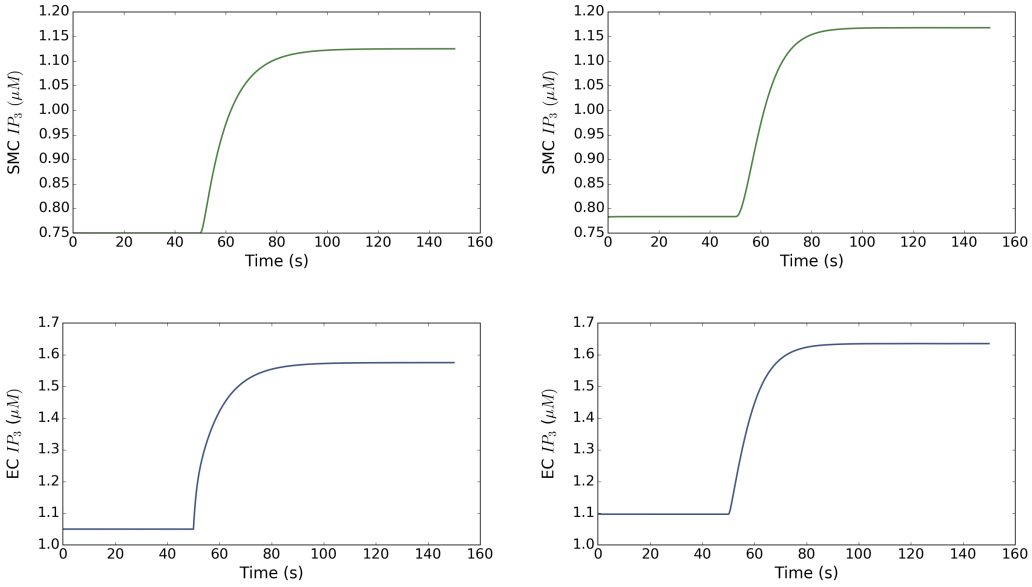

Figure 4.8: IP_3 dynamics in SMCs (top) and ECs (bottom), compared between the original cellular model (left) and that including a detailed IP_3 pathway (right). ATP is introduced at $t = 50s$.

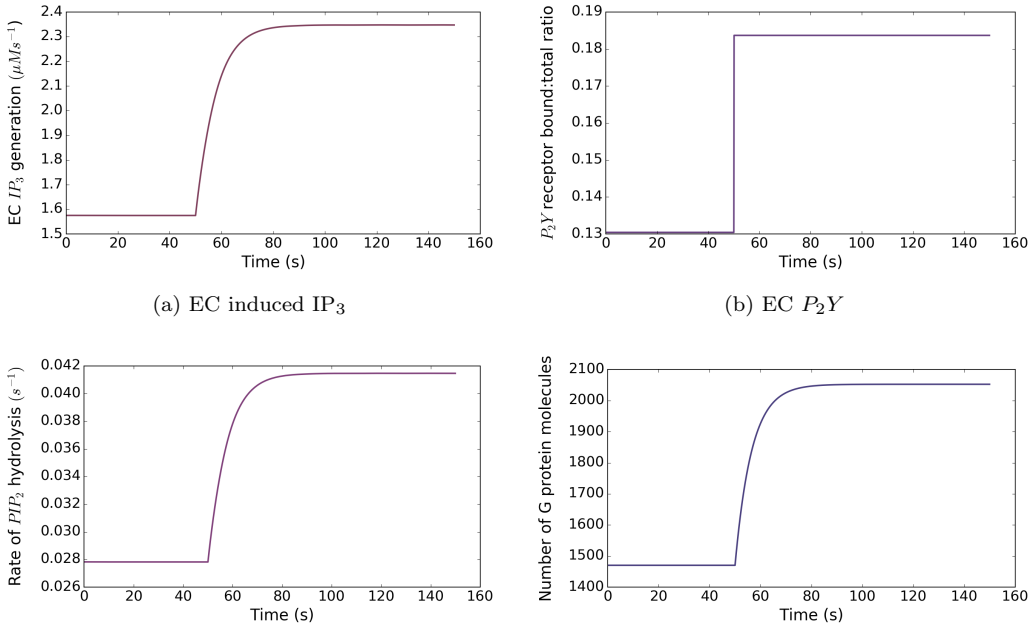

(a) EC induced IP_3

(b) EC P_2Y

(c) EC PIP_2 refreshment

(d) EC G protein

Figure 4.9: Single cell dynamics for a selection of newly added EC fluxes, following the implementation of the detailed IP_3 pathway. ATP is introduced at $t = 50s$.

Ca^{2+} concentrations in both ECs and SMCs are not shown; they are not directly connected to the model modifications.

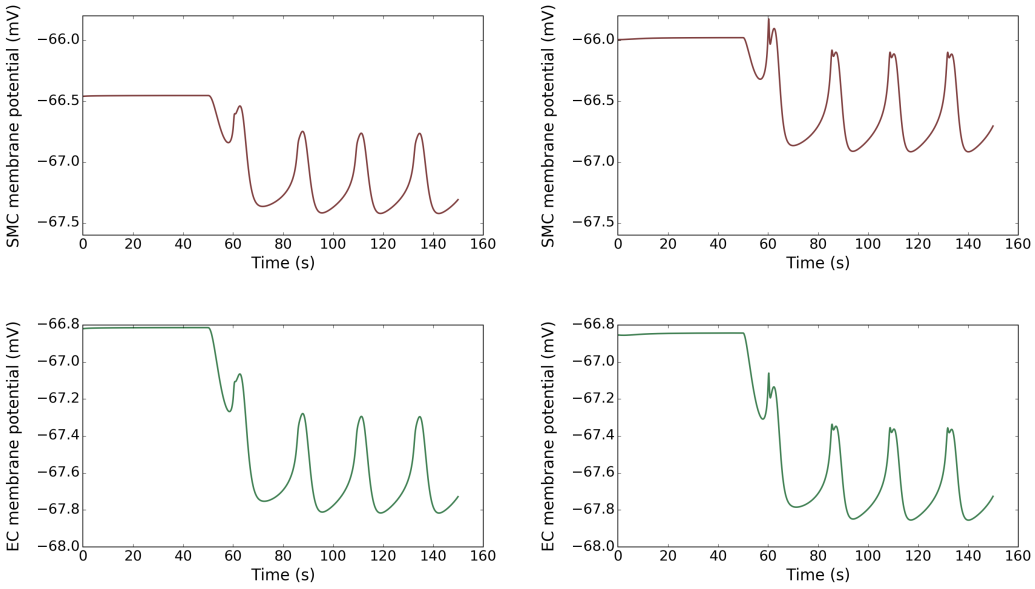

Figure 4.10: Membrane potential in SMCs (top) and ECs (bottom), using Fickian diffusion (left) vs. gap-junction currents (right). ATP is introduced at $t = 50s$.

4.3 Computational Performance

The modifications to this computational component are highly important; they allow current simulations to be conducted at an appropriate (and larger) scale given the available hardware, and provide stepping-stones to improve performance further in the future.

4.3.1 OpenMP

A sequence of experiments were run using OpenMP's `collapse` directive on the two most computationally expensive procedures within our simulations to determine the optimal number of threads for a given problem size. This problem size is the number of cells each core is responsible for, and is controlled using the new variable domain decomposition strategies described in the previous chapter.

For both targeted procedures, the implementations of the `collapse` directive were tested independently with 100-physiological-second simulations. They have different relative computational expenses, and as such might have required a different number of threads for optimal performance. Figure 4.11 shows the results of these tests using a local quad-core desktop machine with 32 gigabytes of RAM. All experiments were run three times and the values averaged, to reduce the effect of noise.

Two, three, and four threads demonstrated the largest reduction in simulation time for both procedures across all tested problem sizes. The reduction was smaller in the case of two threads in the relatively more expensive procedure. These observations may not hold for larger problem sizes. However, the memory available to each node on Fitzroy limited the number of quadrilaterals assigned to each core to approximately 10. Given this machine

was responsible for running the majority of our massively parallel simulations, problem sizes larger than it could accommodate were not considered.

A comparison between the old simulation code and that simultaneously utilising OpenMP in `koenigsberger_ec_explicit` and `koenigsberger_smc_explicit`, as well as the resulting performance improvements, can be seen in Figure 4.12. A reduction in simulation time of up to 27% was obtained when each core was responsible for 16 quadrilaterals—that is 1280 ECs and 3328 SMCs per core. For an eight-to-one quadrilateral:core ratio (the size currently employed in our large-scale simulations on Fitzroy) an improvement of approximately 20% was achieved.

4.3.2 MPI Communication Optimisation

A number of experiments with varying numbers of cores per physiological branch were conducted to measure the effect of grouping communication between cores into fewer, larger messages. The details of this communication strategy, using `MPI_Gather`, is provided in the description of the parallel implementation (Section 3.4). This tested the hypothesis that increasing the number of cores per branch would result in a greater loss of performance in simulations with more frequent communication, despite the total data transferred remaining fixed. In particular, the result of transforming five independent gathers into one five-times the size, for both ECs and SMCs was examined.

Experiments were first conducted on a local machine, where the branch size ranged between 1–64 quadrilaterals, in power of two increments. No measurable difference was found. The same experiments were run again, on the Fitzroy supercomputer, with an increased range of 1–1024 quadrilaterals per branch. In agreement with the previous results, simulation times were not significantly different in those that implemented multiple smaller MPI_Gather calls, compared to those with fewer but larger ones. It is entirely possible that a greater difference could be obtained with greater reduction in the number of smaller gathers. This might be the case, for example, if the single-cell model grows to contain more than five state-variables that require mass communication. However, this number is unlikely to increase dramatically, and so is not considered further here.

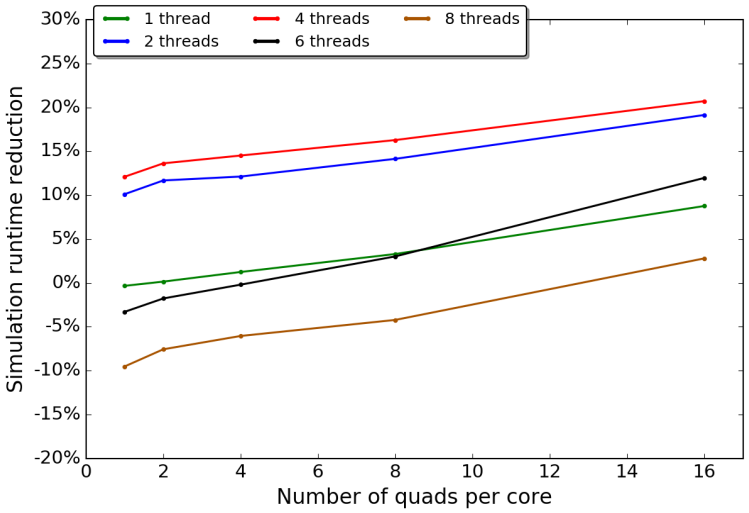

(a) Applying OMP `collapse` to the most expensive procedure, `koenigsberger_ec_explicit`.

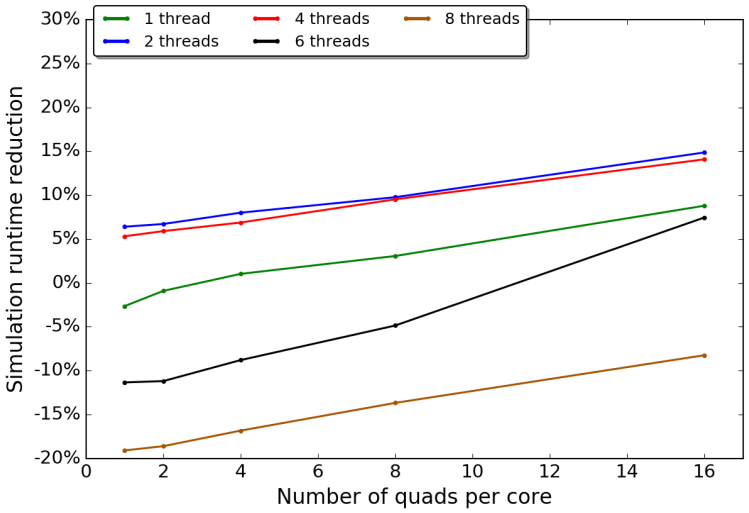

(b) Applying OMP `collapse` to the second most expensive procedure, `koenigsberger_smc_explicit`.

Figure 4.11: Performance of multiple OpenMP threads over increasing problem sizes (quadrilaterals per core). The results for three, five, and seven threads have not been included to aid in visual clarity. Performance is compared to a baseline experiment with one thread and nested for-loops.

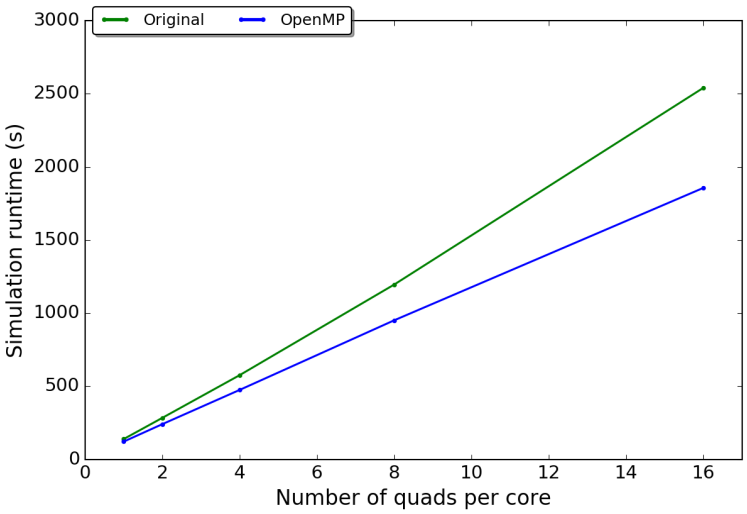

(a) Simulation time of the original code compared to that with OpenMP.

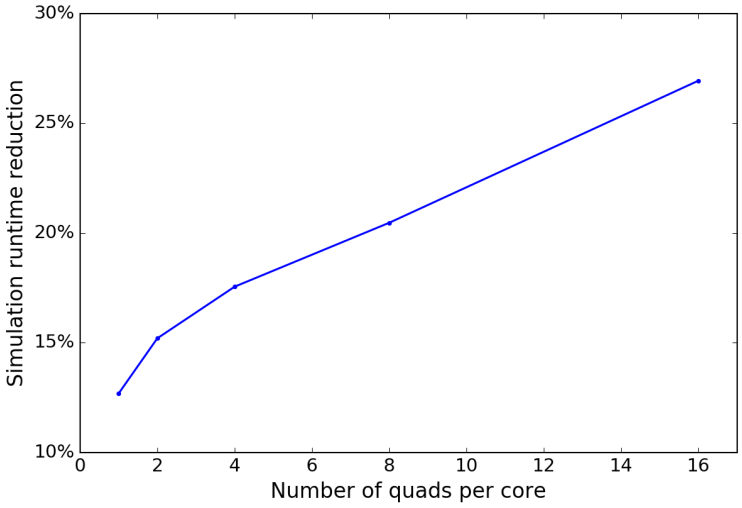

(b) Performance increase with the addition of OpenMP, measured by the resulting reduction in simulation time. Multiple threads were used concurrently in both `koenigsberger_ec_explicit` (four) and `koenigsberger_smc_explicit` (two) procedures.

Figure 4.12: Performance comparison of simulation code without OpenMP to that with it.

4.4 Summary

Massively parallel simulations of arterial geometries with varying bifurcation angles, followed by the supporting extensions to individual components of these simulations, were presented in this chapter.

Macro-scale simulations displayed propagating Ca^{2+} waves in SMCs, and steady-state concentrations of Ca^{2+} in ECs. Particularly complex SMC Ca^{2+} behaviour was observed at the lateral bifurcation seams—waves propagated more slowly, unevenly, less frequently, and over significantly shorter distances. These phenomena were difficult to analyse, given they are presented in 3-D and are time-dependent. Subsequently, post-processing scripts responsible for temporally averaging dynamics and transforming 3-D surfaces to 2-D were created. These provided a different perspective of SMC Ca^{2+} dynamics that allowed us to make new observations. Arterial geometries with wider bifurcation angles contained regions of lower time-averaged Ca^{2+} concentrations compared to those with smaller bifurcation angles. This will be discussed in Chapter 5.

The additions to the cellular model appear to have had little effect on the single-cell dynamics compared with those from the original model. All species displayed steady-state behaviour before the introduction of agonistic ATP, after which many began oscillating. In particular, SMC cytosolic Ca^{2+}, SMC SR Ca^{2+}, and EC/SMC membrane potential began oscillating following the introduction of ATP, while EC cytosolic Ca^{2+}, EC ER Ca^{2+}, and EC/SMC IP_3 concentrations reached new equilibriums. The period of all oscillations has been reduced by approximately 10% following the implementation of the IP_3 pathway.

Finally, modifications to the parallel implementation demonstrated significant performance improvements. The introduction of OpenMP reduced local simulation time by up to 27%, which utilised the method of dynamically assigning the number of cells to each processor core by joining quadrilaterals at runtime.

Chapter 5

Discussion and Conclusions

This chapter discusses the results presented in Chapter 4 under the same three major headings. First, the macro-scale simulations of arterial physiology that are at the core of this research will be examined. The supporting modifications to these simulations will then be analysed, beginning with the extensions to the single-cell model. In particular, the effect these extensions have on current simulations and the implications for future work will be reviewed. The modifications to the parallel implementation will then be discussed, with an emphasis on performance increases and scalability. Where appropriate, the findings are reviewed in the context of related literature. Finally, conclusions are presented, including a consideration of the limitations of the research described here. Suggestions for future work are provided, with a focus on research that can use the tools developed here to enhance our knowledge of atherosclerosis development.

5.1 Macro-scale Simulations

All of the simulations presented in Section 4.1 showed propagating waves of Ca^{2+} in the SMC layer and steady-state concentrations in ECs, following the introduction of lumenal ATP. This agonist binds to endothelial receptors, induces the production of IP3, and consequently the release of Ca^{2+} in both ECs and SMCs. While ECs are non-excitable cells, and their cellular dynamics quickly reach equilibrium, SMCs are excitable, and their Ca^{2+} concentrations can oscillate under certain conditions. Further, strong coupling between SMCs can result in propagating waves of Ca^{2+}. These phenomena have previously been reported in the physiological modelling literature (Koenigsberger et al., 2005; Kapela et al., 2008; Silva et al., 2007; Boileau et al., 2015).

The results from simulations using physiologically accurate ATP input maps were very similar to those using the synthetically generated maps. However, the CFD-based input maps are more physiologically accurate, and so the simulations that used those will be the focus of the remaining discussion.

Complex behaviour in EC and SMC Ca^{2+} dynamics was observed at the lateral bifurcation seams. In particular, these areas exhibited low Ca^{2+} concentrations in ECs, while

Ca^{2+} waves in SMCs propagated in a slower, non-uniform manner, and over significantly shorter distances. In addition, the Ca^{2+} waves within these regions were thinner than the waves elsewhere on the bifurcation segment, with respect to the number of axial SMCs. These phenomena result from lower basal Ca^{2+} concentrations in the corresponding regions. Fewer ATP molecules bind to the endothelial surface and activate G-protein coupled receptors, which results in less phosphorylation of PIP_2 via the membrane-bound enzyme PLC. Consequently, fewer IP_3 molecules bind to IP_3 receptors on the ER, resulting in reduced Ca^{2+} release into the EC cytosol. The relatively low EC IP_3 concentration results in less heterocellular IP_3 diffusion between ECs and SMCs, so that the Ca^{2+} released into SMC cytosol from the SR is also reduced.

A consequence of these irregular Ca^{2+} oscillations and wave propagation is lower Ca^{2+} concentrations in *both* ECs and SMCs over extended periods of time. It has been suggested that low Ca^{2+} concentrations in ECs may contribute to the onset of vascular disease (Plank et al., 2006). There is considerable evidence from the work of Malek et al. (1999) and Chen and Popel (2007) that the production of NO is reduced in areas of low WSS, which in turn leads to endothelial dysfunction (Davignon and Ganz, 2004) and may result in an increased probability of atherogenesis. The (eNOS-mediated) production of NO is a function of cytosolic calcium concentration. As early as 1988, Olesen et al. (1988) found a clear relationship between WSS and calcium-induced potassium currents. It was suggested by Caro et al. (1971) and Ku et al. (1985) that these biochemical changes were related to atherosclerotic regions. Finally, Ca^{2+} is able to move between ECs and SMCs in healthy cellular states, primarily through the Cx40 connexin protein subunit. A concentration change in one layer will therefore affect the other, and so Ca^{2+} dynamics in SMCs should be considered when investigating the onset of vascular disease.

In addition to studying the dynamics of chemical species, the possible localisation of plaque development has been investigated using CFD methods. Pinto and Campos (2016) suggested that areas under arterial bifurcations are susceptible to potential plaque development, due to observed low TAWSS and high RRT values. Dong et al. (2014) presented a more specific hypothesis—that it is these areas under bifurcations with wider angles that are at greater risk of plaque formation.

We observed low Ca^{2+} concentrations in both ECs and SMCs, in regions that CFD research has identified as sites most likely to experience plaque development (Peiffer et al., 2013; Pinto and Campos, 2016; Steinman et al., 2002). Further, we note the low Ca^{2+} concentrations in these areas are more prominent in arterial geometries with wider bifurcation angles, in agreement with the findings of Dong et al. (2014). These results, in conjunction with other findings from the literature, suggest bifurcation angulation may affect the susceptibility of arterial regions to atherosclerosis development through reduced NO production, and subsequent inhibition of atheroprotective conditions.

5.1.1 Limitations

The pinching of cell shape and size at the seams of surface-mesh bifurcations used in the simulations was noted in Section 3.1. This artefact, in combination with the assumption of constant concentrations within each cell (lumped parameter model), created distortions to

SMC Ca^{2+} wave propagation. These distortions can be seen in Figures 4.2, 4.3, and 4.4, and most obviously in the front-on views at $t = 500s$. This behaviour makes analysis of cellular dynamics difficult in this area. It appears as if Ca^{2+} waves propagated slowly before reaching the main steam, due to the size of the local cells, after which their velocity radically increased, which is not physiologically accurate.

For a given mesh, the ECs and SMCs on each quad are aligned orthogonally with respect to each other, where ECs align axially with the flow and the SMCs align circumferentially. They are generated such that they communicate with four neighbouring cells homocellularly, when in fact an EC and SMC can typically communicate with six ECs and SMCs, respectively (Koenigsberger et al., 2005). This communication pattern may affect the Ca^{2+} wave propagation profile, given the limited directions of coupling between each cell. The orientation of both ECs and SMCs would be best described with a statistical distribution, but a simpler and still reasonable improvement to the original alignment would be a brick-tessellation, such that each cell communicates homocellularly with six other cells.

5.2 Single Cell Model

Following the additions of a detailed IP_3 pathway, and gap-junction currents, the single-cell dynamics observed were very similar to those seen using the original model. The only observable differences were in oscillatory frequency and initial conditions. However, the original mathematical model was less physiologically accurate—the assumptions and simplifications that appeared to produce reasonable results would have incurred technical debt into the simulation code in future. Moreover, future simulations should benefit from the flexibility that these additions provide. We are now able to model and control a number of new species. In particular, we have detailed accounts of P_2Y receptors, G protein, and PIP_2 refreshment rates following the implementation of the IP_3 pathway. It is quite possible that a connection exists between the dynamics of one or more of these species, and plaque development. If such a connection were to be found, we would not only be able to model the behaviour of that species, but also manipulate it and observe the effect.

The addition of equations modelling gap-junction currents similarly improves the model's flexibility. These equations consider the movement of Ca^{2+}, K^+, Cl^-, and Na^+, where the concentration of Ca^{2+} is relatively small compared to the others. The dynamics of K^+, Cl^-, and Na^+ are not currently described in the model, and consequently their concentrations are set to constant values. This results in cellular membrane potential displaying near identical behaviour in the original and revised models. However, this might not be the case should we decide to model the dynamics of other ionic species. For example, the concentrations of K^+ across cells do not vary significantly under healthy cellular conditions (Jacobsen et al., 2007), while in certain diseased states they do. In such cases, describing these gap-junction currents would likely produce significantly different results compared with those obtained using Fickian diffusion of membrane potential.

5.2.1 Limitations

Parameters for the various fluxes used in our physiological model were calculated from *in vivo* and *in vitro* experimental data using different animal species. The results they provide should therefore be interpreted broadly, as they are qualitative in nature.

Additions to the model may improve physiological accuracy, but they do so at the cost of simulation runtime. In fact, the solution of ODEs accounts for approximately 50% of the time in any given simulation, so extensions can be computationally expensive. Because of this, it is important to weigh the value of additions to the model against the increased simulation time they incur. At the present time, the importance of modelling a detailed IP_3 pathway and gap-junction currents is believed to outweigh their minor computational costs.

5.3 Parallel Implementation

The balance between code maintainability and efficiency is often quite difficult to achieve, especially within the domain of parallel computing. Obtaining both is certainly the goal, but occasionally sacrifices to one in favour of the other may be necessary. This is particularly so in the case of the recent parallel implementation addition, OpenMP.

The benefits of OpenMP are clearly revealed when it is used to parallelise large sections of code—that is, when the associated computational overhead of creating threads is relatively low compared to the performance increase they provide. Section 4.3 demonstrated this trade-off, showing that both an increase and decrease in performance of our simulations was possible, depending on the number of threads chosen.

The two procedures parallelised with OpenMP were independent of each other, as they described dynamics in two different cell types. This was a natural division which aided maintainability. However, if they were to be joined into one monolithic procedure, the multi-threading performance increase would probably be greater. The same can be said for many of the sections in the simulation code. However, these sacrifices to code maintainability were not made to the research presented in this thesis. They would have introduced technical debt—extra development work generated for the future by accepting the easiest solution in the short term.

5.3.1 Limitations

The problem size per processor core was bound by the hardware on which our simulations were run, and specifically by the amount of memory that was available to each processor core. The improvement to performance using OpenMP in this research was therefore limited. For example, a 27% reduction in simulation time was reported in Section 4.3, using a 16:1 quad:core ratio. In contrast, the machine used to conduct our massively parallel simulations could only accommodate a problem size of 10 quads per core, and such a level of performance increase would not be possible.

5.4 Future Work

Shaikh et al. (2012) introduced multiple coupling cases to early Coupled Cells simulations, to model both healthy and pathological conditions in coupled cells behaviour. These coupling cases were not the focus of the research presented in this thesis—the particular coupling cases modelling unhealthy cellular behaviour already assume mid to late stages of artheroma development. However, future work should include the creation of new coupling cases that reflect initial stages of disease, before plaque formation is observable. Further, these coupling cases should vary both temporally and spatially. The results of the simulations presented in Section 4.1 show specific locations on geometries of abnormal cellular dynamics. Different coupling parameters should be employed at these locations, reflecting potentially emergent dysfunctional cellular communication. This is particularly important, given our simulations span physiological time periods of minutes, while atherosclerotic plaques characteristically develop over time scales of months. Modification of localised communication channels as a function of atypical cellular dynamics, such as significantly lower Ca^{2+} concentrations, would allow us to simulate the progression of vascular disease in relatively short simulations, where physiologically these changes to cellular communication may take months.

Many geometric variations were considered in the study conducted by Lee et al. (2008), among which was bifurcation angulation. This property was chosen for analysis as a result of Dong et al.'s (2014) findings that bifurcations with wider angles are more likely to experience greater flow detachment. However, there exist many other geometric properties, such as bifurcation tortuosity, that are worthy of future exploration. The mesh generation pipeline presented in Section 3.1.1 enables the creation of these various geometries.

A crucial addition to the physiological model will be the endothelial nitric oxide pathway. This pathway describes the production of NO as a result of agonistic molecules within the lumen binding to EC receptors. NO has known athero-protective properties, such as inhibiting the production of various adhesion molecules that encourage the recruitment of monocytes. Following the implementing of this pathway in macro-scale simulations, it will be possible to examine NO dynamics across large sections of ECs, and make more accurate predictions as to the locations of atherosclerotic plaque development.

There is the potential for further improvements to computational performance through significant code restructuring. One such example is to remove all mathematical equations from simulation code, and place them into an external `.ini` file; this would serve to divorce any given physiological model from its implementation. This would allow a developer, not necessarily adept in programming, to make modifications to the model without the risk of damaging code maintainability. The use of `.ini` files could also allow for all independent equations to be solved in parallel, providing a significant performance increase.

5.5 Conclusions

The primary research question proposed in Chapter 1 related to the effect arterial bifurcation angulation has on the onset of atherosclerosis. The literature on this topic was

reviewed to understand what previous work has revealed, and why it has not yet been possible to describe precisely how different geometries may be predisposed to plaque formation. Aspects of vascular disease have been studied, such as micro-scale cellular dynamics, and CFD simulations on vessel geometries. However, concurrently using physiologically accurate micro-scale cellular dynamics with varying macro-scale geometries, and incorporating CFD from these geometries as agonistic input had not been attempted. To conduct simulations that would aid in answering the main research question, a number of improvements to the existing coupled cells model were necessary.

The macro-scale simulations presented oscillatory and steady state behaviour in SMC and EC species, respectively. These results were expected following the literature review. Moreover, significantly lower Ca^{2+} concentrations were observed in areas under the bends of bifurcations, in both ECs and SMCs. The particular SMC Ca^{2+} dynamics in these areas was difficult to analyse at any given time point; waves propagated more slowly, non-uniformly, and over significantly shorter distances. Post-processing, in the form of time-averaging, was applied to better understand the emergent properties of these dynamics. This showed significantly lower Ca^{2+} concentrations over time at the lateral bifurcation seams compared to the other surface regions of the arterial vessel. In conjunction with findings reported in the literature, these results suggest arterial bifurcations containing wider angles may indeed influence the development of atherosclerosis, by means of disturbed flow and consequently lower EC and SMC Ca^{2+} concentrations.

To accommodate our current macro-scale simulations on the available hardware, and provide greater scalability for future work, modifications to the parallel implementation were performed. These primarily consisted of including OpenMP, and the ability to specify the desired problem size per processor core at runtime. To realise the greatest benefit of introducing OpenMP to the simulation code, the profiling tool TAU was used. This enabled the targeting of the most computationally expensive procedures during simulations for performance improvement.

The single-cell dynamics of our simulations were examined, and compared with other mathematical models of physiology in the related literature. To ensure our simulations were physiologically accurate and flexible for future studies, the underlying model was extended to include a detailed IP_3 pathway, and gap-junction currents that replace Fickian diffusion of membrane potential. We have not yet experimented with the newly-modelled species, but note the potential to do so in future simulations.

A flexible method of creating arterial surface-meshes was introduced, capable of generating surfaces with wide ranges of complexity and geometric variations described by input centrelines. A method of creating synthetic centrelines was introduced, able to emulate many geometric complexities including vessel planarity, varying diameters for branches within the geometry, and the angles between any of these branches. These geometries are required for our own simulations, as well as for the CFD simulations that generate the input ATP maps.

This research has provided a flexible simulation platform that allows for the investigation of cellular dynamics within geometrically varying, multi-scale arterial sections. The potential influence of bifurcation angulation on plaque development has been studied, and

the investigation of many other phenomena is now possible. Other variations to vascular geometry have been highlighted for immediate future work to provide a more comprehensive understanding of atherosclerosis development. Finally, all additions and modifications made to this platform were designed and implemented to promote scalability and further improvement. Future simulations of arterial physiology, including surface-meshes that span the entire coronary tree, should benefit from these extensions.

Bibliography

Asakura, T. and Karino, T. (1990). Flow Patterns and Spatial Distribution of Atherosclerotic Lesions in Human Coronary Arteries. *Circulation Research*, 66: 1045–1066.

Ayachit, U. (2015). *The ParaView Guide: A Parallel Visualization Application*. Kitware, Inc., USA.

Bedner, P., Niessen, H., Odermatt, B., Kretz, M., Willecke, K., and Harz, H. (2006). Selective permeability of different connexin channels to the second messenger cyclic AMP. *Journal of Biological Chemistry*, 281(10): 6673–6681.

Bennett, M. R., Farnell, L., and Gibson, W. (2005). A Quantitative Model of Purinergic Junctional Transmission of Calcium Waves in Astrocyte Networks. *Biophysical Journal*, 89(4): 2235–2250.

Bloor, M. I. G. and Wilson, M. J. (1989). Generating blend surfaces using partial differential equations. *Computer-Aided Design*, 21(3): 165–171.

Boileau, E., Parthimos, D., and Nithiarasu, P. (2015). An Extended Computational Framework to Study Arterial Vasomotion and Its Links to Vascular Disease. *Biomedical Technology*, 11(3): 129–144.

Brisset, A. C., Isakson, B. E., and Kwak, B. R. (2009). Connexins in vascular physiology and pathology. *Antioxidants & Redox Signaling*, 11(2): 267–82.

Burnier, L., Fontana, P., Angelillo-Scherrer, A., and Kwak, B. R. (2009). Intercellular communication in atherosclerosis. *Physiology (Bethesda, Md.)*, 24: 36–44.

Caro, C., Pedley, T., Schoroter, R., and Seed, W. (2012). *The Mechanics of the Circulation*, volume 71. Oxford University Press, Oxford.

Caro, C. G., Fitz-Gerald, J. M., and Schroter, R. C. (1971). Atheroma and Arterial Wall Shear Observation, Correlation and Proposal of a Shear Dependent Mass Transfer Mechanism for Atherogenesis. *Proceedings of the Royal Society of London B: Biological Sciences*, 177(1046): 109–133.

Cecchi, E., Giglioli, C., Valente, S., Lazzeri, C., Gensini, G. F., Abbate, R., and Mannini, L. (2011). Role of hemodynamic shear stress in cardiovascular disease. *Atherosclerosis*, 214(2): 249–256.

Chen, K. and Popel, A. S. (2007). Vascular and perivascular nitric oxide release and transport: Biochemical pathways of neuronal nitric oxide synthase (NOS1) and endothelial nitric oxide synthase (NOS3). *Free Radical Biology and Medicine*, 42(6): 811–822.

Comerford, A. and David, T. (2008). Computer model of nucleotide transport in a realistic porcine aortic trifurcation. *Annals of Biomedical Engineering*, 36(7): 1175–1187.

Davignon, J. and Ganz, P. (2004). Role of Endothelial Dysfunction in Atherosclerosis. *Circulation*, 109(23): 27–32.

de Groot, E. (2004). Measurement of arterial wall thickness as a surrogate marker for atherosclerosis. *Circulation*, 109(23_suppl_1): III33–III38.

Dong, J., Sun, Z., Inthavong, K., and Tu, J. (2014). Fluid-structure interaction analysis of the left coronary artery with variable angulation. *Computer Methods in Biomechanics and Biomedical Engineering*, 18(14): 1500–1508.

Emerson, G. G. and Segal, S. S. (2000). Electrical coupling between endothelial cells and smooth muscle cells in hamster feed arteries: role in vasomotor control. *Circulation Research*, 87(6): 474–479.

Fry, D. L. (1969). Certain Chemorheologic Considerations Regarding the Blood Vascular Interface with Particular Reference to Coronary Artery Disease. *Circulation*, 40(5S4): IV–38–IV–57.

Goldbeter, A., Dupont, G., and Berridge, M. J. (1990). Minimal model for signal-induced Ca2+ oscillations and for their frequency encoding through protein phosphorylation. *Proceedings of the National Academy of Sciences of the United States of America*, 87(4): 1461–1465.

Gropp, W., Hoefler, T., Thakur, R., and Lusk, E. (2014). *Using Advanced MPI: Modern Features of the Message-Passing Interface*. MIT Press, Cambridge, Massachusetts.

Hai, C. M. and Murphy, R. A. (1988). Cross-bridge phosphorylation and regulation of latch state in smooth muscle. *American Journal of Physiology - Cell Physiology*, 254(1): C99 LP – C106.

Hindmarsh, A. C., Brown, P. N., Grant, K. E., Lee, S. L., Serban, R., Shumaker, D. E., and Woodward, C. S. (2005). SUNDIALS: Suite of nonlinear and differential/algebraic equation solvers. *ACM Transactions on Mathematical Software (TOMS)*, 31(3): 363–396.

Jacobsen, J. C. B., Aalkjaer, C., Nilsson, H., Matchkov, V. V., Freiberg, J., and Holstein-Rathlou, N.-H. (2007). A model of smooth muscle cell synchronization in the arterial wall. *American Journal of Physiology - Heart and Circulatory Physiology*, 293(March 2007): H229–H237.

Johny, J. P. (2016). *Modulating factors of intracellular calcium dynamics in vascular smooth muscle cell*. Doctoral thesis, University of Canterbury, Christchurch, New Zealand.

Johny, J. P., Plank, M. J., and David, T. (2017). Importance of Altered Levels of SERCA, IP3R, and RyR in Vascular Smooth Muscle Cell. *Biophysical Journal*, 112(2): 265–287.

Kapela, A., Bezerianos, A., and Tsoukias, N. M. (2008). A mathematical model of Ca2+ dynamics in rat mesenteric smooth muscle cell: Agonist and NO stimulation. *Journal of Theoretical Biology*, 253(2): 238–260.

Koenigsberger, M., Sauser, R., Beny, J.-L., Meister, J.-J., Bény, J.-L., and Meister, J.-J. (2005). Role of the endothelium on arterial vasomotion. *Biophysical Journal*, 88(June): 3845–3854.

Koenigsberger, M., Sauser, R., Lamboley, M., Bény, J.-L., and Meister, J.-J. (2004). Ca2+ dynamics in a population of smooth muscle cells: modeling the recruitment and synchronization. *Biophysical Journal*, 87(July): 92–104.

Ku, D. N., Giddens, D. P., Zarins, C. K., and Glagov, S. (1985). Pulsatile flow and atherosclerosis in the human carotid bifurcation. Positive correlation between plaque location and low oscillating shear stress. *Arteriosclerosis*, 5: 293–302.

Lee, D. and Chiu, J. J. (1992). A numerical simulation of intimal thickening under shear in arteries. *Biorheology*, 29: 337–351.

Lee, S. W., Antiga, L., Spence, J. D., and Steinman, D. A. (2008). Geometry of the carotid bifurcation predicts its exposure to disturbed flow. *Stroke*, 39(8): 2341–2347.

Lemon, G., Gibson, W. G., and Bennett, M. R. (2003). Metabotropic receptor activation, desensitization and sequestration - I: Modelling calcium and inositol 1,4,5-trisphosphate dynamics following receptor activation. *Journal of Theoretical Biology*, 223(1): 93–111.

Lerman, A. and Zeiher, A. M. (2005). Endothelial function: Cardiac events. *Circulation*, 111(3): 363–368.

Libby, P. (2002). Inflammation in atherosclerosis. *Nature*, 420(6917): 868–74.

Longest, P. W., Kleinstreuer, C., Truskey, G. A., and Buchanan, J. R. (2003). Relation between near-wall residence times of monocytes and early lesion growth in the rabbit aorto-celiac junction. *Annals of Biomedical Engineering*, 31(1): 53–64.

Malek, A. M., Alper, S. L., and Izumo, S. (1999). Hemodynamic Shear Stress and Its Role in Atherosclerosis. *Journal of the American Medical Association*, 282(21): 2035–2042.

Mendis, S., Puska, P., and Norrving, B. (2011). *Global Atlas on Cardiovascular Disease Prevention and Control*. World Health Organization, Geneva, 1 edition.

Mohamied, Y., Sherwin, S. J., and Weinberg, P. D. (2016). Understanding the Fluid Mechanics Behind Transverse Wall Shear Stress. *Journal of Biomechanics*, 50: 102–109.

National Heart Lung and Blood Institute (2016). What Is Atherosclerosis? `https://www.nhlbi.nih.gov/health/health-topics/topics/atherosclerosis`.

Olesen, S. P., Clapham, D. E., and Davies, P. F. (1988). Haemodynamic shear stress activates a K+ current in vascular endothelial cells. *Nature*, 331(6152): 168–170.

Parthimos, D., Edwards, D. H., and Griffith, T. M. (1999). Minimal model of arterial chaos generated by coupled intracellular and membrane Ca2 + oscillators. *American Journal of Physiology*, 277(22): H1119–H1144.

Peiffer, V., Sherwin, S. J., and Weinberg, P. D. (2013). Does low and oscillatory wall shear stress correlate spatially with early atherosclerosis? A systematic review. *Cardiovascular Research*, 99(2): 242–250.

Pinto, S. I. S. and Campos, J. B. L. M. (2016). Numerical study of wall shear stress-based descriptors in the human left coronary artery. *Computer Methods in Biomechanics and Biomedical Engineering*, 19(13): 1443–1455.

Plank, M. J., Wall, D. J. N., and David, T. (2006). Atherosclerosis and calcium signalling in endothelial cells. *Progress in Biophysics and Molecular Biology*, 91(3): 287–313.

Rackauskas, M., Verselis, V. K., and Bukauskas, F. F. (2007). Permeability of homotypic and heterotypic gap junction channels formed of cardiac connexins mCx30.2, Cx40, Cx43, and Cx45. *American Journal of Physiology - Heart and Circulatory Physiology*, 293(3): 1729–1736.

Seymour, G., Elliot, W., K., Z. C., Regina, S., and J., K. G. (1987). Compensatory Enlargement of Human Atherosclerotic Coronary Arteries. *New England Journal of Medicine*, 316(22): 1371–1375.

Shaikh, M. A. (2011). *Models of coupled smooth muscle and endothelial cells.* Doctoral thesis, University of Canterbury, Christchurch, New Zealand.

Shaikh, M. A., Wall, D. J. N., and David, T. (2012). Macro-scale phenomena of arterial coupled cells: a massively parallel simulation. *Journal of The Royal Society Interface*, 9(70): 972–987.

Shende, S. S. and Malony, A. D. (2006). The Tau Parallel Performance System. *International Journal of High Performance Computing Applications*, 20(2): 287–311.

Silva, H. S., Kapela, A., and Tsoukias, N. M. (2007). A mathematical model of plasma membrane electrophysiology and calcium dynamics in vascular endothelial cells. *American Journal of Physiology - Cell Physiology*, 293(1): C277–93.

Steinman, D. A., Thomas, J. B., Ladak, H. M., Milner, J. S., Rutt, B. K., and David Spence, J. (2002). Reconstruction of carotid bifurcation hemodynamics and wall thickness using computational fluid dynamics and MRI. *Magnetic Resonance in Medicine*, 47(1): 149–159.

Tabor, G., Weller, H. G., Jasak, H., and Fureby, C. (1998). A tensorial approach to computational continuum mechanics using object-oriented techniques. *Computers in Physics*, 12(6): 620–631.

Warboys, C. M., Eric Berson, R., Mann, G. E., Pearson, J. D., and Weinberg, P. D. (2010). Acute and chronic exposure to shear stress have opposite effects on endothelial permeability to macromolecules. *American Journal of Physiology - Heart and Circulatory Physiology*, 298(6): H1850–H1856.

Wentzel, J. J., Chatzizisis, Y. S., Gijsen, F. J. H., Giannoglou, G. D., Feldman, C. L., and Stone, P. H. (2012). Endothelial shear stress in the evolution of coronary atherosclerotic plaque and vascular remodelling: Current understanding and remaining questions. *Cardiovascular Research*, 96(2): 234–243.

World Health Organisation (2015). The top 10 causes of death. `http://www.who.int/mediacentre/factsheets/fs310/en/`.

Yin, Y., Lim, K. H., Weinbaum, S., Chien, S., and Rumschitzki, D. S. (1997). A model for the initiation and growth of extracellular lipid liposomes in arterial intima. *American Journal of Physiology - Heart and Circulatory Physiology*, 272(2): H1033 LP – H1046.

Appendices

Appendix A

Coupled Cells model

The definition of all fluxes used in the physiological model and their parameters are provided in this section. This includes intra- and intercellular fluxes for both ECs and SMCs in the original model.

A.1 Intracellular SMC Fluxes

IP_3-induced Ca^{2+} release:

$$J_{\mathrm{IP}_3} = F\frac{\mathcal{I}^2}{K_r^2 + \mathcal{I}^2}. \tag{A.1}$$

Ca^{2+}-induced Ca^{2+} release from SR into cytosol:

$$J_{\mathrm{CICR}} = C\frac{s^2}{s_c^2 + s^2}\frac{c^4}{c_c^4 + c^4}. \tag{A.2}$$

Ca^{2+} transfer back into the SR via the Ca^{2+}-activated SERCA pump:

$$J_{\mathrm{SR\_uptake}} = B\frac{c^2}{c_b^2 + c^2}. \tag{A.3}$$

Ca^{2+} leak from SR:

$$J_{\mathrm{leak}} = Ls. \tag{A.4}$$

Influx of extracellular Ca^{2+} via VOCC:

$$J_{\mathrm{VOCC}} = G_{\mathrm{Ca}}\frac{v - v_{\mathrm{Ca}_1}}{1 + \mathrm{e}^{-\left[\left(v - v_{\mathrm{Ca}_2}\right)/R_{\mathrm{Ca}}\right]}}. \tag{A.5}$$

Efflux of Ca^{2+} via the Na^+/Ca^{2+} exchanger:

$$J_{\mathrm{Na/Ca}} = G_{\mathrm{Na/Ca}}\frac{c}{c + c_{\mathrm{Na/Ca}}}\left(v - v_{\mathrm{Na/Ca}}\right). \tag{A.6}$$

Removal of intracellular Ca^{2+} through the PMCA pump:

$$J_{\text{eff}} = Dc\left(1 + \frac{v - v_d}{R_d}\right). \tag{A.7}$$

Function of the Ca^{2+}-activated K^+ channels determined by the cytosolic Ca^{2+} concentration:

$$K_{\text{activation}} = \frac{(c + c_\omega)^2}{(c + c_\omega)^2 + \beta e^{-[(v - v_{Ca_3})/R_K]}}. \tag{A.8}$$

Potassium efflux through the plasma membrane-bound BK_{Ca} channels, where ω is the open channel probability of the Ca^{2+}-activated channels expressed as a function of $K_{activation}$:

$$J_K = G_{\text{K}}\omega\,(v - v_k)\,. \tag{A.9}$$

Influx of chloride ions caused by the plasma membrane depolarisation:

$$J_{Cl} = G_{\text{Cl}}\,(v - v_{Cl})\,. \tag{A.10}$$

Constant rate efflux of potassium through the Na^+/K^+ pump:

$$J_{\text{Na/K}} = F_{Na/K}. \tag{A.11}$$

Linear IP_3 concentration degradation:

$$J_{degrade} = k\mathcal{I}. \tag{A.12}$$

A.2 Intracellular EC Fluxes

IP_3-induced Ca^{2+} release:

$$\tilde{J}_{\text{IP}_3} = \tilde{F}\frac{\tilde{\mathcal{I}}^2}{\tilde{K}_r^2 + \tilde{\mathcal{I}}^2}. \tag{A.13}$$

Ca^{2+}-induced Ca^{2+} release from ER into cytosol:

$$\tilde{J}_{\text{CICR}} = \tilde{C}\frac{\tilde{s}^2}{\tilde{s}_r^2 + \tilde{s}^2}\frac{\tilde{c}^4}{\tilde{c}_c^4 + \tilde{c}^4}. \tag{A.14}$$

Ca^{2+} transfer back into the ER via the Ca^{2+}-activated SERCA pump:

$$\tilde{J}_{\text{ER\_uptake}} = \tilde{B}\frac{\tilde{c}^2}{\tilde{c}_b^2 + \tilde{c}^2}. \tag{A.15}$$

Ca^{2+} leak from ER:

$$\tilde{J}_{\text{leak}} = \tilde{L}\tilde{s}. \tag{A.16}$$

Removal of intracellular Ca^{2+} through the PMCA pump:

$$\tilde{J}_{\text{eff}} = \tilde{D}\tilde{c}. \tag{A.17}$$

Calcium influx through non-selective cation channels:

$$\tilde{J}_{\text{cation}} = \tilde{G}_{\text{cat}} \left(E_{\text{Ca}} - \tilde{v}\right) \times \frac{1}{2} \left(1 + \tanh\left(\frac{\log_{10} \tilde{c} - \tilde{m}_{3_{\text{cat}}}}{\tilde{m}_{4_{\text{cat}}}}\right)\right). \tag{A.18}$$

Constituent currents determined by the potassium efflux through large and small Ca^{2+}-activated channels:

$$\tilde{J}_{\text{K}} = \tilde{G}_{\text{tot}} \left(\tilde{v} - \tilde{v}_{\text{K}}\right) \left(\tilde{J}_{\text{BK}_{\text{Ca}}} - \tilde{J}_{\text{SK}_{\text{Ca}}}\right), \tag{A.19}$$

where

$$\tilde{J}_{\text{BK}_{\text{Ca}}} = \frac{0.4}{2} \left(1 + \tanh\left(\frac{\left(\log_{10} \tilde{c} - \tilde{c}_K\right)\left(\tilde{v} - \tilde{b}_K\right) - \tilde{a}_{K1}}{\tilde{m}_{3b}\left(\tilde{v} + \tilde{a}_{K2}\left(\log_{10} \tilde{c} - \tilde{c}_K\right) - \tilde{b}_K\right)^2 + \tilde{m}_{4\text{b}}}\right)\right) \tag{A.20}$$

and

$$\tilde{J}_{\text{SK}_{\text{Ca}}} = \frac{0.6}{2} \left(1 + \tanh\left(\frac{\log_{10} \tilde{c} - \tilde{m}_{3s}}{\tilde{m}_{4s}}\right)\right). \tag{A.21}$$

Residual current comprising an inward sodium or potassium current and an outward chloride current:

$$\tilde{J}_{\text{residual}} = \tilde{G}_{\text{R}} \left(\tilde{v} - \tilde{v}_{\text{rest}}\right). \tag{A.22}$$

Linear IP_3 concentration degradation:

$$\tilde{J}_{degrade} = \tilde{k}\tilde{\mathcal{I}}. \tag{A.23}$$

A.3 Model Parameters

Table A.1 provides the parameters for a single SMC, while Table A.2 provides the parameters for a single EC.

F	Maximal rate of activation-dependent calcium influx	0.23 μM s^{-1}
K_r	Half saturation constant for agonist-dependent calcium entry	1 μM
G_{Ca}	Whole cell conductance for VOCCs	0.00129 μM mV^{-1} s^{-1}
v_{Ca1}	Reversal potential for VOCCs	100 mV
v_{Ca2}	Half-point of the VOCC activation sigmoidal	−24 mV
R_{Ca}	Maximum slope of the VOCC activation sigmoidal	8.5 mV
$G_{Na/Ca}$	Whole cell conductance for Na^+/Ca^{2+} exchange	0.00316 μM mV^{-1} s^{-1}
$c_{Na/Ca}$	Half-point for activation of Na^+/Ca^{2+} exchange by Ca^{2+}	0.5 μM
$v_{Na/Ca}$	Reversal potential for the Na^+/Ca^{2+} exchanger	−30 mV
B	SR uptake rate constant	2.025 μM s^{-1}
c_b	Half-point of the SERCA activation sigmoidal	1.0 μM
C	CICR rate constant	55 μM s^{-1}
s_c	Half-point of the CICR Ca^{2+} efflux sigmoidal	2.0 μM
c_c	Half-point of the CICR activation sigmoidal	0.9 μM
D	Rate constant for Ca^{2+} extrusion by the ATPase pump	0.24 s^{-1}
v_d	Intercept of voltage dependence of extrusion ATPase	−100 mV
R_d	Slope of voltage dependence of extrusion ATPase	250 mV
L	Leak from SR rate constant	0.025 s^{-1}
g	Scaling factor relating net movement of ion fluxes to the membrane potential (inversely related to cell capacitance)	1970 mV^{-1} μM
$F_{Na/K}$	Net whole cell flux via the Na^+–K^+–ATPase	0.0432 μM s^{-1}
G_{Cl}	Whole cell conductance for Cl^- current	0.00134 μM mV^{-1} s^{-1}
v_{Cl}	Reversal potential for Cl^- channels	−25 mV
G_K	Whole cell conductance for K^+ efflux	0.00446 μM mV^{-1} s^{-1}
v_K	Reversal potential for K^+	−94 mV
λ	Rate constant for net K_{Ca} channel opening	45
c_ω	Translation factor for Ca^{2+} dependence of K_{Ca} channel activation sigmoidal	0 μM
β	Translation factor for membrane potential dependence of K_{Ca} channel activation sigmoidal	0.13 μM^2
v_{Ca_3}	Half-point for the K_{Ca} channel activation sigmoidal	−27 mV
R_K	Maximum slope of the K_{Ca} activation sigmoidal	12.0 mV
k	Rate constant of IP_3 degradation	0.1 s^{-1}

Table A.1: SMC model parameters as described by Koenigsberger et al. (2005).

$\tilde{F}$	Maximal rate of activation-dependent calcium influx	0.23 μM s^{-1}
$\tilde{K}_r$	Half saturation constant for agonist-dependent calcium entry	1 μM
$\tilde{B}$	ER uptake rate constant	0.5 μM s^{-1}
$\tilde{c}_b$	Half-point of the SERCA activation sigmoidal	1.0 μM
$\tilde{C}$	CICR rate constant	5 μM s^{-1}
$\tilde{s}_c$	Half-point of the CICR Ca^{2+} efflux sigmoidal	2.0 μM
$\tilde{c}_c$	Half-point of the CICR activation sigmoidal	0.9 μM
$\tilde{D}$	Rate constant for Ca^{2+} extrusion by the ATPase pump	0.24 s^{-1}
$\tilde{L}$	Leak from SR rate constant	0.025 s^{-1}
$\tilde{k}$	Rate constant of IP_3 degradation	0.1 s^{-1}
$\tilde{G}_{cat}$	Whole cell cation channel conductivity	0.66 μM μV^{-1} s^{-1}
$\tilde{E}_{Ca}$	Ca^{2+} equilibrium potential	50 μV
$\tilde{m}_{3_{cat}}$		-0.18 μM
$\tilde{m}_{4_{cat}}$		0.37 μM
$\tilde{J}_0$	Constant calcium influx	0.029 μM s^{-1}
$\tilde{C}_m$	Membrane capacitance	25.8 pF
$\tilde{G}_{tot}$	Total potassium channel conductivity	6927 pS
$\tilde{v}_K$	K^+ equilibrium potential	-80 μV
$\tilde{a}_{K1}$		53.3 μM uV
$\tilde{a}_{K2}$		53.3 μV μM^{-1}
$\tilde{b}_K$		-80.8 μV
$\tilde{c}_K$		-0.4 μM
$\tilde{m}_{3b}$		1.32×10^3 μM μV^{-1}
$\tilde{m}_{4b}$		0.30 μM μV^{-1}
$\tilde{m}_{3s}$		-0.28 μM
$\tilde{m}_{4s}$		0.389 μM
$\tilde{G}_R$	Residual current conductivity	955 pS
$\tilde{v}_{rest}$	Membrane resting potential	-31.1 μV

Table A.2: EC model parameters as described by Koenigsberger et al. (2005).

		Case 1	Case 2	Case 3	Case 4
Homocellular	g	1000	1000	1000	1000
	$\tilde{g}$	1000	1000	1000	0
	p_{Ca}	0.05	0.05	0.05	0.05
	$\tilde{p}_{Ca}$	0.05	0.05	0.05	0
	p_{IP_3}	0.05	0.05	0.05	0.05
	$\tilde{p}_{IP_3}$	0	0	0.05	0.05
Heterocellular	G	50.0	50.0	50.0	0
	$\tilde{G}$	50.0	50.0	50.0	0
	P_{Ca}	0	0.05	0.05	0
	$\tilde{P}_{Ca}$	0	0.05	0.05	0
	P_{IP_3}	0.05	0.05	0.05	0.05
	$\tilde{P}_{IP_3}$	0.05	0.05	0.05	0.05

Table A.3: Coupling parameters for four intercellular communication configurations; Cases 1 and 2 simulate healthy paracrine communication, while Cases 3 and 4 simulate pathological cases, with early and progressive atherosclerotic lesions respectively. Taken from Shaikh et al. (2012).

Symbol	Definition	Value	Notes
δ	G-protein intrinsic activity parameter	$1.234 \cdot 10^{-3}$	Lemon et al. (2003)
K_a	G-protein activation rate	$0.017\ s^{-1}$	Lemon et al. (2003)
K_d	G-protein deactivation rate	$0.15\ s^{-1}$	Lemon et al. (2003)
N_a	Avogadro's constant	$6.02252 \cdot 10^{23} mol^{-1}$	–
$unitcon_B$	Constant to convert $mol/\mu m$ into μM	10^{21}	–
α	Effective signal gain parameter	$2.781 \cdot 10^{-5} s^{-1}$	Lemon et al. (2003)
K_{Ca}	Dissociation Constant for Ca^{2+} binding to PLC	$0.4\ \mu M$	Lemon et al. (2003)
r_r	Rate of PIP_2 replenishment	$10\ s^{-1}$	Lemon et al. (2003)
$PIP_{2_{tot}}$	Total number of PIP_2 molecules	$5.0 \cdot 10^7$	
$G_{prot_{tot}}$	Total number of G-protein molecules	$1.0 \cdot 10^5$	Lemon et al. (2003)
k_{deg}	IP_3 degradation rate	$1.25\ s^{-1}$	Lemon et al. (2003)

Table A.4: Model parameter values used in the IP_3 pathway.

Symbol	Definition	Value	Reference
$A_{average}$	Averaged area of cells in contact	Varies on the cells in contact	See text
$P_{general}$	Standard value of permeability	5×10^{-8} m/s. P_x is calculated by scaling this value according to the following ratio: 1:0.8:0.6 for K^+: Ca^{2+}: Na^+: Cl^-	Jacobsen et al. (2007)
F	Faraday Constant	96487.0 C/mol	-
R	Universal Gas Constant	8314.0 $mJ/molK$	-
T	Absolute temperature	293.0 K	Kapela et al. (2008)
σ	Fraction of circumference directed toward neighbouring cell	0.15 for homocellular coupling, 0.05 for heterocellular coupling	Jacobsen et al. (2007) and see text
$[Na^+]_{cyt,smc}$	Intracellular concentration of Sodium in SMCs	8.4 mM	Kapela et al. (2008)
$[K^+]_{cyt,smc}$	Intracellular concentration of Potassium in SMCs	140.0 mM	Kapela et al. (2008)
$[Cl^-]_{cyt,smc}$	Intracellular concentration of Chloride in SMCs	59.4 mM	Kapela et al. (2008)
$[Na^+]_{cyt,ec}$	Intracellular concentration of Sodium in ECs	8.3 mM	Silva et al. (2007)
$[K^+]_{cyt,ec}$	Intracellular concentration of Potassium in ECs	128.0 mM	Silva et al. (2007)
$[Cl^-]_{cyt,ec}$	Intracellular concentration of Chloride in ECs	87.0 mM	Silva et al. (2007)

Table A.5: Gap junction current parameter values.

Appendix B

Published Work

To date, the work presented in this thesis has contributed to a published journal paper and two extended abstracts accepted for oral presentation at the international conference Virtual Physiological Human (VPH), held in Amsterdam, The Netherlands. References and brief descriptions of these works are provided below.

B.1 Journal Paper

Zakkaroff, C., Moore, S., Dowding, S., and David, T. (2017). 3D time-varying simulations of Ca(2+) dynamics in arterial coupled cells: A massively parallel implementation. *International Journal for Numerical Methods in Biomedical Engineering*, 33(2).

This journal paper extended the 2D coupled-cell simulations by Shaikh et al. (2012) to use idealised 3D arterial bifurcation surface meshes. The introduction of these 3D surfaces allowed for agonist input maps to be generated with CFD simulations, as well as synthetically.

B.2 Extended Abstracts

Zakkaroff, C., Dowding, S., Kenny, A., and David, T. (2016). Effect of Bifurcation Angles on Arterial Coupled Cell Dynamics : Massively Parallel Simulations. In Hoekstra, A., editor, *Virtual Physiological Human*, The Netherlands, Amsterdam.

This extended abstract presented preliminary results on the effect bifurcation angulation has on coupled arterial physiology. The geometries were planar, the cellular model did not include gap-junction currents, and the input ATP maps were synthetically created to approximate what CFD might have provided.

Dowding, S., Zakkaroff, C., and Johny, J. P. (2016). In Silico Simulations of In Vitro Vasodilation Experiments. In Hoekstra, A., editor, *Virtual Physiological Human*, The Netherlands, Amsterdam.

This work examined *in vitro* experiments described by Emerson and Segal (2000), and attempted to replicate the results with our *in silico* simulations. Two stimuli were applied to isolated arteries: 0.8 nA current was injected into an EC, and 0.8 nA injected into an SMC, to learn whether direct electrical coupling can promote relaxation and contraction in the vessel.